Flat optics with dispersion-engineered metasurfaces

Wei Ting Chen ✉, *Alexander Y. Zhu and Federico Capasso* ✉

Abstract | Control over the dispersion of the refractive index is essential to the performance of most modern optical systems. These range from laboratory microscopes to optical fibres and even consumer products, such as photography cameras. Conventional methods of engineering optical dispersion are based on altering material composition, but this process is time-consuming and difficult, and the resulting optical performance is often limited to a certain bandwidth. Recent advances in nanofabrication have led to high-quality metasurfaces with the potential to perform at a level comparable to their state-of-the-art refractive counterparts. In this Review, we introduce the underlying physical principles of metasurface optical elements (with a focus on metalenses) and, drawing on various works in the literature, discuss how their constituent nanostructures can be designed with a highly customizable effective index of refraction that incorporates both phase and dispersion engineering. These metasurfaces can serve as an essential component for achromatic optics with unprecedented levels of performance across a broad bandwidth or provide highly customized, engineered chromatic behaviour in instruments such as miniature aberration-corrected spectrometers. We identify some key areas in which these achromatic or dispersion-engineered metasurface optical elements could be useful and highlight some future challenges, as well as promising ways to overcome them.

Optical dispersion results from the variation in the index of refraction of a material with the frequency of incident light. Accurate control over this property is crucial in numerous industrial and research applications. For example, it mitigates pulse spreading in optical fibres, which are the backbone of modern telecommunications[1,2], enables pulse shaping in ultra-fast laser optics[3–5] and ensures faithful image reproduction in imaging systems by reducing chromatic aberrations. This has enabled various technologies that underlie widely used commercial products, ranging from state-of-the-art microscopes to cameras, as well as various metrology instruments that are indispensable to modern manufacturing processes.

Historically, after Sir Isaac Newton used a prism to disperse sunlight into different colours (that is, wavelengths)[6,7], he realized that a similar effect, due to the inherent dispersion in glasses, led to image blurring in lenses. Because it is impossible to make a glass with a constant index of refraction for all wavelengths of light, he resorted to using only reflective mirrors in his design of telescopes. In the 1730s, it was discovered that a doublet lens made of flint and crown glasses comprising different types and amounts of metal oxides in a fused-silica matrix could substantially reduce chromatic aberrations[8]. This is because introducing an additional lens made of a slightly different material provides an extra degree of freedom to compensate for the dispersion of the entire system. Nevertheless, it was not until the late 1800s that the combined efforts of Carl Zeiss, Ernst Abbe and Otto Schott in achromatic lens design and glass-making techniques led to the development of multi-wavelength, colour-corrected microscope objectives that are still widely used today[6,9].

This example highlights the difficulties inherent to the approach of correcting chromatic aberration by altering material composition. A continuous range of desired dispersion values cannot be achieved over a large bandwidth, and allowed combinations of glasses and dopants must be explored extensively, which is very time-consuming and challenging in terms of fabrication. To date, there are only about a thousand types of different glasses that are readily available from major glass suppliers such as Schott, Hoya and Ohara. This number includes overlaps, in which glasses from one company possess very similar optical properties to those from another.

In mobile-phone cameras, the camera module typically consists of about six plastic aspherical lenses made of different materials to correct both chromatic and monochromatic aberrations. Precise alignment of these lenses is a great challenge, and the difficulty increases with the number of lenses. For instance,

Harvard John A. Paulson School of Engineering and Applied Sciences, Harvard University, Cambridge, MA, USA.

✉*e-mail: weitingchen@seas.harvard.edu; capasso@seas.harvard.edu*

https://doi.org/10.1038/s41578-020-0203-3

Leica Inc. developed an instrument that weighs six tons to automatically align a microscope objective of less than a kilogram. Although many companies are able to mass-produce the injection-moulded plastic lenses, only a few can perform precise alignment with high yield for mobile-phone cameras. Together, these factors represent a technological and manufacturing challenge to the further shrinking of the form factor of high-end, achromatic, optical components.

In sharp contrast to traditional refractive optics, optical metasurfaces consisting of sub-wavelength nanostructures can introduce an effective refractive index and dispersion that are dictated mainly by the geometrical parameters and arrangement of the structures, rather than by the material's composition. Recent advances in nanofabrication have gradually improved the focusing efficiency of metasurfaces up to approximately 90% in some cases, which makes them viable candidates for a variety of practical applications. Importantly, they have a uniform height profile, resulting in an essentially flat surface topology. This substantially reduces the alignment challenges, as one can adapt well-developed techniques that are widely used in semiconductor foundries[10]. As such, metasurfaces are well positioned to act as a platform for designing dispersion-tailored optical components, and they can either function as independent optical elements or work in tandem with refractive optics to achieve achromaticity. In this Review, we first briefly summarize common design and fabrication methods for metasurfaces, with an emphasis on metalenses. We then introduce several novel design and computational techniques that can lead to multifunctional metasurfaces and substantially improve their efficiency. Finally, we highlight some recent developments in dispersion-engineered metasurface optics and provide an outlook for the near future.

For ease of discussion and comparison, in this Review, the focusing efficiency of a metalens is defined as the power contained within a focal spot divided by the power of incident light. This definition is necessary because, unlike in refractive lenses, in metalenses, not all transmitted light can be focused. Some light is transmitted without picking up the desired phase profile; it can also be diffracted to unwanted angles, causing background noise and secondary foci, which, in turn, lead to the generation of haze and ghost images, respectively. The power of the focal spot is usually measured in a confocal microscope set-up by placing an iris at the image plane with a diameter equal to about twice the diameter of an ideal Airy disk. The relative efficiency is defined similarly, but is normalized to the power of transmitted light. The difference between these two terms is that the relative efficiency does not take into account the reflection from nanostructures.

Metalenses across the spectrum of light

Depending on how its constituent nanostructures are shaped and arranged, a dielectric metasurface can perform different functions, such as lensing[11–13], phase retardation[14–16] or beam deflection[17–20], to name a few. Metalenses are usually made of a material that is lossless within the bandwidth of interest and possesses a high index of refraction. The latter is crucial to confine light strongly within the nanostructures and improve overall device efficiency; it also greatly alleviates fabrication challenges by lowering the height of nanostructure required for imparting a 2π phase delay. The fabrication process is typically based on either electron-beam or optical lithography, followed by dry etching or film deposition[15,21]. Methods for scaling up and improving the throughput of the fabrication process are discussed in a subsequent section.

Some examples of experimentally demonstrated, high-efficiency metalenses comprising different materials and operating in various regions of the electromagnetic spectrum, ranging from the ultraviolet to the mid-infrared, are illustrated in FIG. 1. At visible wavelengths, typical materials used are TiO_2 (REFS[21,22]), GaN (REFS[23,24]), single-crystal silicon[25–27] and Si_3N_4 (REFS[28,29]) (FIG. 1b). TiO_2 metalenses with high focusing efficiencies of up to 86% at incident wavelength $\lambda = 405$ nm have been demonstrated[30]. GaN metalenses have recently attracted attention, owing to the relatively well-developed fabrication techniques used in the production of blue light-emitting diodes and because they provide a potential platform to study the interaction between nanostructures and a gain medium[31–33]. A GaN metalens with up to 92% focusing efficiency at $\lambda = 532$ nm has been reported[24]. Because single-crystal silicon exhibits much lower optical loss than amorphous silicon, an immersion metalens with high numerical aperture (up to 1.48) and with 67% focusing efficiency at $\lambda = 532$ nm has been fabricated using this material[34] (FIG. 1b). In this metalens, the single-crystal silicon nanostructures can be in direct contact with the liquid to increase the working distance and avoid efficiency losses, thanks to the high index of refraction compared with that of TiO_2 immersion metalenses[35]. In the ultraviolet[36–38], HfO_2 metalenses operating down to a record wavelength of 266 nm with a focusing efficiency of 60 % were recently demonstrated[39] (FIG. 1a). By contrast, at near-infrared wavelengths, amorphous silicon is the most suitable material[40,41]. Amorphous-silicon metalenses with focusing efficiency as high as 70% and 82% at operating wavelengths of $\lambda = 850$ nm and 1,550 nm, respectively, have been demonstrated[42,43] (FIG. 1c), and metasurface-polarization components with a transmission of up to 97% have been reported[15]. For mid-infrared applications, both Si (REFS[44–46]) and PbTe (REFS[47,48]) have been used (FIG. 1d); these metalenses can have focusing efficiencies of approximately 75%[45,47].

The aforementioned metalenses have efficiencies that vary with the choice of material, because fabrication constraints dictate the minimum feature size and periodicity; the distinct refractive indices of the materials used also result in different degrees of light confinement at the various operating wavelengths. Furthermore, the constituent structures impart a phase delay by different mechanisms (such as resonant effects, propagation or the geometric phase, BOX 1). Together, these factors contribute to the disparity in efficiency figures of metalenses; however, there is room for progress by improving fabrication processes and exploring more sophisticated structure geometries. These examples illustrate that

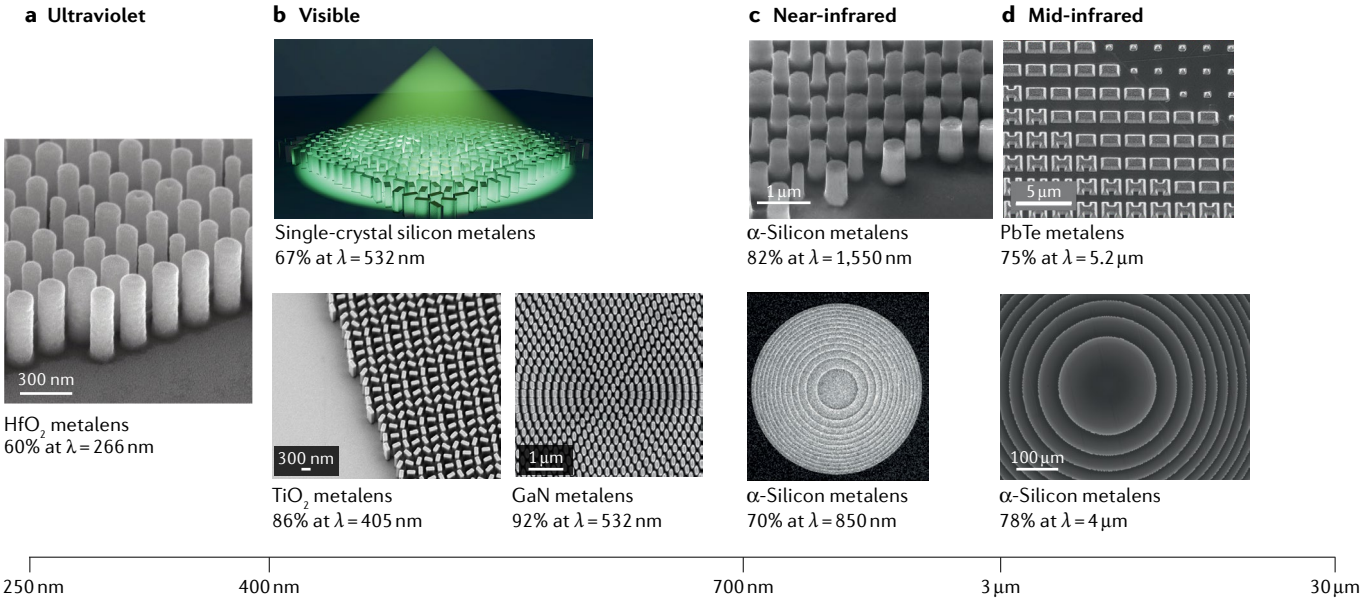

Fig. 1 | **Chromatic metalenses across the electromagnetic spectrum.** High-refractive-index, low-loss dielectric materials such as titanium oxide, gallium nitride, crystalline and amorphous silicon, and lead telluride are suitable candidates for fabricating efficient metalenses at different operating wavelengths. The fabrication processes are readily adapted from modern semiconductor-fabrication techniques. For each metalens, the focusing efficiency and operating wavelength, λ, are specified. **a** | HfO_2 metalens operating in the ultraviolet range. **b** | Metalenses operating in the visible range. **c** | α-Silicon metalenses operating in the near-infrared range. **d** | PbTe and α-silicon metalenses operating in the mid-infrared range. Panel **a** adapted from REF.[39], CC BY 4.0. Panel **b** top adapted with permission from REF.[24], ACS; panel **b** lower left reprinted with permission from REF.[30], AAAS; panel **b** lower right adapted with permission from REF.[34], ACS. Panel **c** top reprinted with permission from REF.[42], IEEE; panel **c** lower panel adapted from REF.[43], Springer Nature Limited. Panel **d** top adapted with permission from REF.[45], Wiley-VCH; lower panel adapted from REF.[47], CC BY 4.0.

metalenses with largely similar design and fabricated with similar techniques can be adapted to various frequency regions for high-end optical components.

Metasurfaces design principles

A typical three-step design flow chart for metasurfaces is shown in FIG. 2. The process starts with the calculation of the target-phase profile $\Phi(x,y)$ at a design wavelength λ_d (x and y represent spatial coordinates along the device surface, FIG. 2a). In general, the goal is to impart a spatially dependent phase delay to incident light in order to shape the transmitted wavefront. The target-phase profile is usually obtained by using either ray tracing or a Fourier-optics method to implement the functions found in various optical elements, such as beam deflectors, lenses and holograms. Without loss of generality, here, we consider the target-phase profile of a metalens (it can be substituted for the phase profile of any other optical component) that focuses a normally incident plane wave to a diffraction-limited spot[49]:

$$\Phi(r) = -\frac{2\pi}{\lambda_d}\left(\sqrt{r^2+f^2} - f\right) \quad (1)$$

with $r = \sqrt{x^2+y^2}$ the radial coordinate and f the focal length. This phase profile possesses a decreasing phase delay from the centre of the metalens to its edge, which compensates for the difference in optical-path lengths and ensures that the transmitted rays from different radial coordinates interfere constructively at the focal spot. However, in many practical scenarios in which multiple other aberrations need to be corrected (such as coma, distortion, astigmatism and field curvature)[50,51], it is challenging to write down an analytical expression for the target-phase profile. More advanced algorithms or lens-design software packages are essential for metasurface devices such as doublet metalenses[41,52] and metasurface spectrometers[53–57]. For instance, the commercial ray-tracing software OpticStudio from Zemax Inc. approximates a target-phase profile for a rotationally symmetric element as:

$$\Phi(r) = \sum_n a_n \left(\frac{r}{R}\right)^{2n} \quad (2)$$

where R is a normalization factor. To describe the phase profiles of many free-form elements, the expression:

$$\Phi(x,y) = \sum_{mn} a_{mn} x^m y^n \quad (3)$$

can be used instead. The coefficients a_n and a_{mn} are used in the software to optimize performance with a customizable figure of merit, such as the wavefront-aberration function, which is defined as the optical-path difference between the actual wavefront and an ideal spherical wavefront.

The next step is to build up a library of nanostructures (FIG. 2b) using full-wave simulation solvers to connect a given structure geometry to the phases that

it can provide. Common choices of nanostructures are circular pillars or nanofins, whose geometric parameters (for example, width and length) are varied to cover a range of 2π phase delays with high transmission. The optical behaviour of a nanofin can be intuitively understood as that of a miniature waveplate (BOX 1). Under circularly polarized incident illumination, $(1 \pm i)^{T}$ (where T represents the matrix transpose and the positive sign denotes left-handed polarized light), the transmitted electric field can be described by the Jones vector[58]:

$$\frac{t_l + t_s}{2}\begin{pmatrix}1\\ \pm i\end{pmatrix} + \frac{t_l - t_s}{2}\exp(\pm i2\theta)\begin{pmatrix}1\\ \mp i\end{pmatrix} \quad (4)$$

Equation 4 can be understood as follows: part of the polarization state of the transmitted light acquires opposite handedness and gets a phase shift of $\arg(\frac{t_l - t_s}{2}) \pm 2\theta$, whereas the remaining part of the transmitted light maintains its polarization and experiences a phase shift of $\arg\left(\frac{t_l + t_s}{2}\right)$. arg denotes the argument of a complex number, and t_l and t_s are the transmission coefficients for incident light linearly polarized along the long and short axes of the nanofin, respectively, and are wavelength-dependent complex numbers. The phase delay of $\pm 2\theta$ is known as the geometric or the Pancharatnam–Berry phase[59–62]; note that the sign of the acquired phase depends on the incident circular polarization (incident light with left-handed circular polarization picks up a positive phase). An anisotropic nanofin can, therefore, impart a precise and relative phase delay from 0 to 2π purely by rotation (FIG. 2b). The length and width of the nanofin are usually chosen such that the phase difference between t_l and t_s is π at the design wavelength λ_d. In this case, the nanofin behaves as an ideal half-waveplate, and the transmission amplitude

Box 1 | Nanostructure-induced phase delays

When light propagates through a nanostructure, a portion is confined inside the nanostructure, while the rest leaks to the surrounding material. This is similar to what happens in a waveguide. Therefore, an intuitive way to understand the optical properties of a nanofin is to treat it as a miniature, truncated waveguide[180]. Owing to the anisotropic geometry of the nanofin, an incident, linearly polarized beam experiences different effective indices of refraction, n_l and n_s, when it passes through the long and short axes of the nanofin, respectively. Panel **a** of the figure shows the simulated effective refractive indices n_l and n_s calculated by the MODE solver of Lumerical for a TiO_2 nanofin array arranged in a square lattice of 400 nm. The length and width of each nanofin are 250 and 80 nm, respectively. When the incident light is polarized along the long axis, it experiences a larger effective index of refraction (red curve). This is because most of the electric-field intensity (shown in panel **b**) is localized inside the TiO_2 nanofin (compare subplot I and subplot III). The effective index of refraction depends on the wavelength, which leads to dispersion. For polarization along the short axis, the majority of the electric field is in air when the incident wavelength is 700 nm (subplot IV); thus, the effective index of refraction is close to unity. The anisotropy of this structure leads to different transmission along the long and short axes, t_l and t_s, respectively; the transmission can be written as:

$$t = |t|\exp\left[i\frac{2\pi}{\lambda}\left(n_{eff} - 1\right)h\right]$$

where λ is the incident wavelength in vacuum, h the height of the nanofin and n_{eff} its effective index of refraction. The nanofin, therefore, acts like a waveplate, and its Jones matrix can be described by $\begin{bmatrix}t_l & 0\\ 0 & t_s\end{bmatrix}$. If the nanofin is rotated by an angle θ with respect to its long axis, the transmitted field is given by:

$$\begin{bmatrix}E_x^{out}\\ E_y^{out}\end{bmatrix} = R(\theta)\begin{bmatrix}t_l & 0\\ 0 & t_s\end{bmatrix}R(-\theta)\begin{bmatrix}E_x^{in}\\ E_y^{in}\end{bmatrix}$$
$$= \left(\frac{t_l + t_s}{2}\begin{bmatrix}1 & 0\\ 0 & 1\end{bmatrix} + \frac{t_l - t_s}{2}\begin{bmatrix}\cos(2\theta) & \sin(2\theta)\\ \sin(2\theta) & -\cos(2\theta)\end{bmatrix}\right)\begin{bmatrix}E_x^{in}\\ E_y^{in}\end{bmatrix}$$

The phase of the transmitted light as a function of wavelength for a TiO_2 nanofin array with a height of 600 nm is shown in panel **c** for light polarized along the short and long axes of the fins (red and blue squares, respectively). The solid curves are calculated based on the waveguide approximation with the effective indices of refraction shown in panel **a**, whereas the squares are results from full-wave finite-difference time-domain simulations. The results agree well, except for short wavelengths. The disagreement between a simplified waveguide model and full-wave finite-difference time-domain simulations can result from multiple mechanisms, such as the excitation of high-order waveguide modes, Bloch modes and resonances[12,181–184]. The origin of the waveguide and Bloch modes and of their interaction in complex nanostructures are discussed in REFS[86,185].

Other mechanisms can also be used to modulate the phase. Typical dielectric particles with sizes smaller than half the incident wavelength exhibit both electric and magnetic dipolar resonances. Careful engineering of these resonances so that they coincide and interfere destructively at the same wavelength can eliminate backscattering (this is known as Kerker's condition) and has been shown to impart a 2π phase delay and result in efficient transmission[186,187]. Plasmonic resonances and waveguides can also be used to realize metasurfaces with high efficiency in the infrared[188,189]. For the low-frequency region, spoof plasmons can be used to control phase delays[190,191].

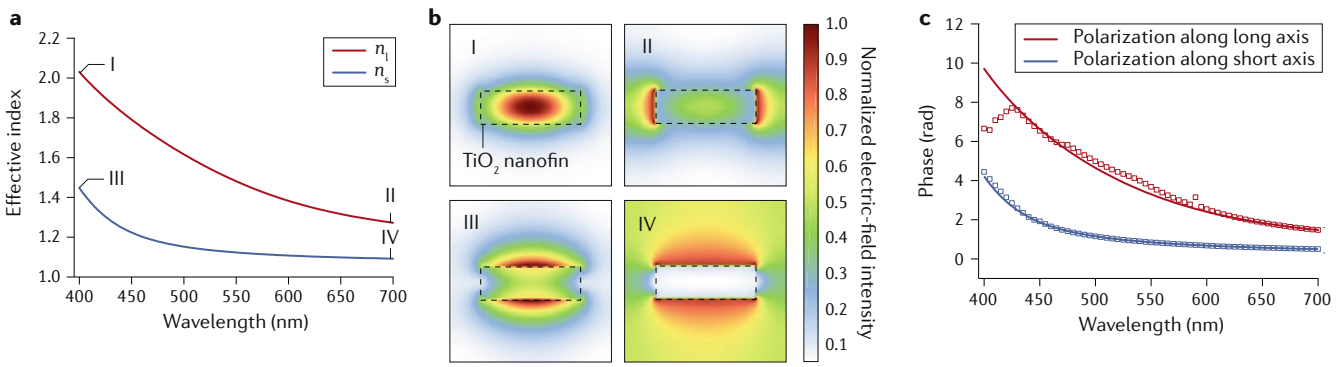

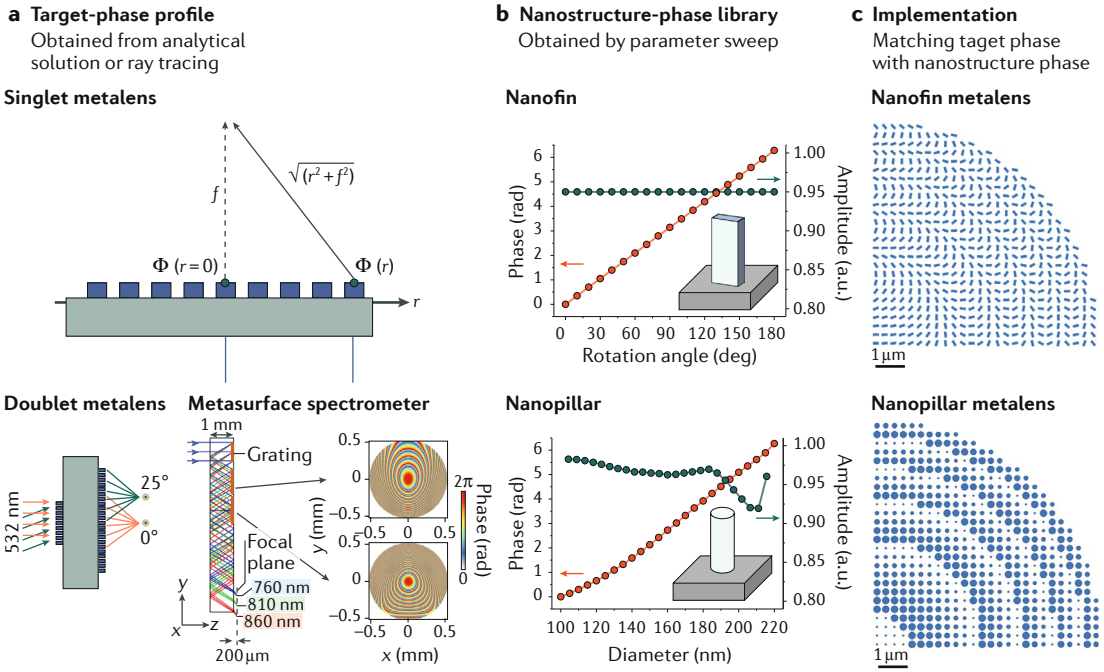

Fig. 2 | **Flow chart for designing a metasurface. a** | The target-phase profile is obtained through an analytical expression in closed form or through series expansions derived from ray-tracing software. For the singlet metalens, the phase profile $\Phi(r)$ can be simply calculated by $\Phi(r) + \frac{2\pi}{\lambda_d}\sqrt{r^2+f^2} = \Phi(0) + \frac{2\pi}{\lambda_d}f$. The equals sign implies that the rays from different lens coordinates r have to arrive at the focus in phase; $\Phi(0)$ can be assumed to be zero, because phase is relative. The phase profile for the bottom two cases (doublet metalens and metasurface spectrometer) is more complicated, especially for the metasurface spectrometer, whose phase profile is not rotationally symmetric. The doublet metalens ensures diffraction-limited focusing over a large field of view of up to 50°. The free-form metasurfaces of the metasurface spectrometer correct aberrations for high spectral resolution. **b** | A library of nanostructures with their corresponding phases and higher-order dispersion terms is established through full-wave electromagnetic solvers. The first subplot shows the transmitted amplitude and phase imparted by a nanofin, depending on its rotation angle for the case of left-handed, circularly polarized light. The second subplot shows phase and amplitude control through the variation of the diameter of a nanopillar. Both subplots show amplitude and phase for a given incident wavelength. **c** | The phases of elements from the library are matched to the target phase through optimization algorithms to determine the best overall fit for all elements across the metasurface. The top views of two metalenses implemented based on geometric (top) and propagation (bottom) phases are shown. The insets in panel **a** of the doublet and spectrometer metalenses adapted with permission from REF.[52], ACS, and from REF.[53], CC BY 4.0.

of $\frac{t_l - t_s}{2}$ at λ_d is maximized. It is also possible to design a nanofin working as an ideal achromatic waveplate by stacking several layers of nanofins[63,64]. In addition, catenary and meniscus structures are found to possess large, high-efficiency bandwidths[65,66].

In Eq. 4, because the sign of the acquired geometric phase depends on the helicity of the incident light, metasurfaces imparting a geometric phase are commonly thought to be intrinsically polarization-sensitive, with their function changing with incident polarization. This limitation can be overcome by judicious design. For instance, a polarization-insensitive and achromatic metalens has recently been demonstrated by limiting the rotations of nanofins to $\theta = 0°$ or 90° to eliminate the conjugated values of $e^{\pm i2\theta}$ resulting from the geometric phase[67]. Beyond lenses, polarization-insensitive metasurface beam splitters and holograms based on the geometric phase can also be realized when their far-field intensity distribution is centrosymmetric[68,69]. It is also possible to eliminate the dependence on polarization if at least four geometric-phase lenses are cascaded[70]. For designs based on isotropic nanostructures, t_l and t_s are equal. Accordingly, the second term in Eq. 4 vanishes and one needs to impart a phase delay, which, in the case of nanopillars, can be done by changing the diameter (FIG. 2b).

The last step of metasurface design is the digitization of the target phase $\Phi(x,y)$ and identification of a nanostructure from the established library that imparts a phase φ_n (n represents the index of a chosen nanostructure in the library) matching $\Phi(x_i,y_i)$ as closely as possible. This fit needs to be optimized through an algorithm. This process is repeated for all the metasurface coordinates. Two layouts of metalenses consisting of circular pillars and nanofins are shown in FIG. 2c. The circular pillars have larger diameters towards the centre, and this pattern is repeated in a periodic way, because the target phase is wrapped back every 2π. Similarly, in the geometric-phase metalens, the nanofins are rotated periodically. Because the size of a metalens is usually on the order of millimetres to centimetres, the number of constituent nanostructures can be very large, owing to their sub-wavelength size and spacing. An efficient algorithm is, therefore, required to produce layout files

for nanolithography machines. By utilizing azimuthal symmetry and efficient coding language, the file size of a centimetre-scale metalens can be compressed from approximately 9 gigabytes to only 24 megabytes[71,72].

Limitations of conventional metasurface design. The design approach described above is based on simulating each library nanostructure at normal incidence with periodic boundary conditions (FIG. 2b). The inverse of the periodicity equals the sampling rate of the target-phase profile. For accurate and efficient implementation of target-phase profile, the Nyquist sampling criterion needs to be fulfilled, that is, a 2π phase variation with spatial coordinates needs to be sampled by at least two nanostructures[11,35]. This design approach assumes that the interaction between adjacent nanostructures in a metasurface device is similar to that in the periodic approximation. This means that the target-phase profile must change slowly with spatial coordinates and, therefore, the nanostructure geometry should not change too rapidly. This approximation also ignores the actual coupling between adjacent nanostructures; it, thus, not appropriate for components with high numerical aperture, for which the required phase gradient is large.

More careful consideration of the vectorial properties of the electromagnetic wave scattered off the nanostructures is required for the efficient steering of light to large angles[73–75]. In addition, the phase imparted by each individual nanostructure depends on the angle; thus, the efficiency or functionality of a metasurface varies with the angle of incidence. Recently, this spatial dispersion was exploited by designing sophisticated nanostructures to realize a meta-hologram capable of showing distinct images at different incidence angles[76]. A metalens that can perform 1D Fourier transfer with large angles of incidence up to 60° has been demonstrated[77]. A reflective metasurface waveplate whose retardance varies from half-wavelength to quarter-wavelength with incidence angle has also been reported[78].

Although most metasurface components can be designed by ray tracing, it is impractical to use ray tracing to design multifunctional metasurfaces whose target-phase profiles are so complicated that the selection of nanostructures becomes counter-intuitive. A wave-optics-based method to obtain the target phase and a better way to select proper nanostructures based on inverse design is presented in REF.[79]. Examples including a two-layered achromatic metalens, a colour-multiplexed hologram and a ten-layered metasurface acting as a neural network for pattern recognition were proposed and verified by simulations. Inverse design can be used to better select nanostructures for multifunctional metasurfaces[80]; an interesting example is a lens capable of focusing light with different angles of incidence to the same point using isotropic TiO_2 nanopillars that are 600 nm tall[80].

Topology-optimized metalenses

In recent years, there has been increasing interest in topology optimization combined with adjoint and gradient-descent methods for metalens design[81–84]. This approach allows the topology of the metasurface to change in a free-form way, opening up a large design space, while converging comparatively quickly to an optimal solution. The process begins by defining a region (usually the entire metasurface, which can be either single-layered or multilayered) consisting of discrete cells whose permittivity needs to be optimized (FIG. 3a). The permittivity ε of each cell can be a number between unity, if the surrounding environment is air, and the permittivity of the chosen material, $\varepsilon_{material}$. The challenge is to quickly and efficiently determine how a change in permittivity in any given cell affects the figure of merit F (that is, $\frac{\partial F}{\partial \varepsilon}$), which, for metalenses, is typically defined as the intensity of the electric field at the focus, $|\vec{E}(\vec{r}_0)|^2$ (REF.[85]). The obvious brute-force approach is to change the permittivity of each cell and run a simulation to determine the impact on the figure of merit. However, this approach is costly in terms of computation time; this is where the adjoint method kicks in. Based on the reciprocity of light, only two full-field simulations are required to obtain $\frac{\partial F}{\partial \varepsilon}$. If we use the metalens with plane-wave incidence as an example, the forward simulation gives the electric field at the focus, $\vec{E}(\vec{r}_0)$, and in the optimization region, $\vec{E}_{\text{forward}}(x', y', z')$. Subsequently, in the adjoint simulation, a dipole with its amplitude, phase and polarization determined by the value of $\vec{E}(\vec{r}_0)$ from the forward simulation emits a spherical wave towards the optimization region, after which the electric field $\vec{E}_{\text{adjoint}}(x', y', z')$ is recorded (FIG. 3a, lower panel). The inner product of $\vec{E}_{\text{forward}}(x', y', z')$ and $\vec{E}_{\text{adjoint}}(x', y', z')$, together with some constants that depend on how F was defined, determines $\frac{\partial F}{\partial \varepsilon}$. The new distribution of permittivity can, therefore, be predicted by a gradient-descent method as $\varepsilon_{\text{new}} = \varepsilon_{\text{old}} + g\frac{\partial F}{\partial \varepsilon}$, where g is a spatially dependent scalar function. Subsequently, the new permittivity $\varepsilon_{\text{new}}(x', y')$ passes through various functions to slowly adjust the value of permittivity to 1 or $\varepsilon_{material}$ (a process called binarization) and to remove geometric features that are too challenging to fabricate before the next iteration[85,86].

Although topology optimization utilizes the adjoint method to shorten the time needed for each iteration, it is still time-consuming to design a large metalens, because it normally takes a few hundred iterations to converge. Some approximations are, therefore, still necessary if one wants to utilize topology optimization to design a metalens with a diameter larger than 100λ. One possibility is to design cylindrical metalenses (focusing incident light to a line, akin to conventional cylindrical lenses) and limit the constituent nanostructures to nanoridges, so that only 2D full-wave simulations are required. The metalens is then divided into sections, and simulation and optimization are performed section by section with periodic boundary conditions or perfectly matched layers. This approach is referred to as the local approximation. The local approximation applies regardless of whether topology optimization is used. A schematic showing how the local approximation is performed is shown in FIG. 3b: each section uses a linear phase to approximate a target phase and scatters incident light to a designed angle[87]. For a 200-μm-diameter metalens designed to work at $\lambda_d = 640$ nm, the local approximation was used in conjunction with topology optimization to

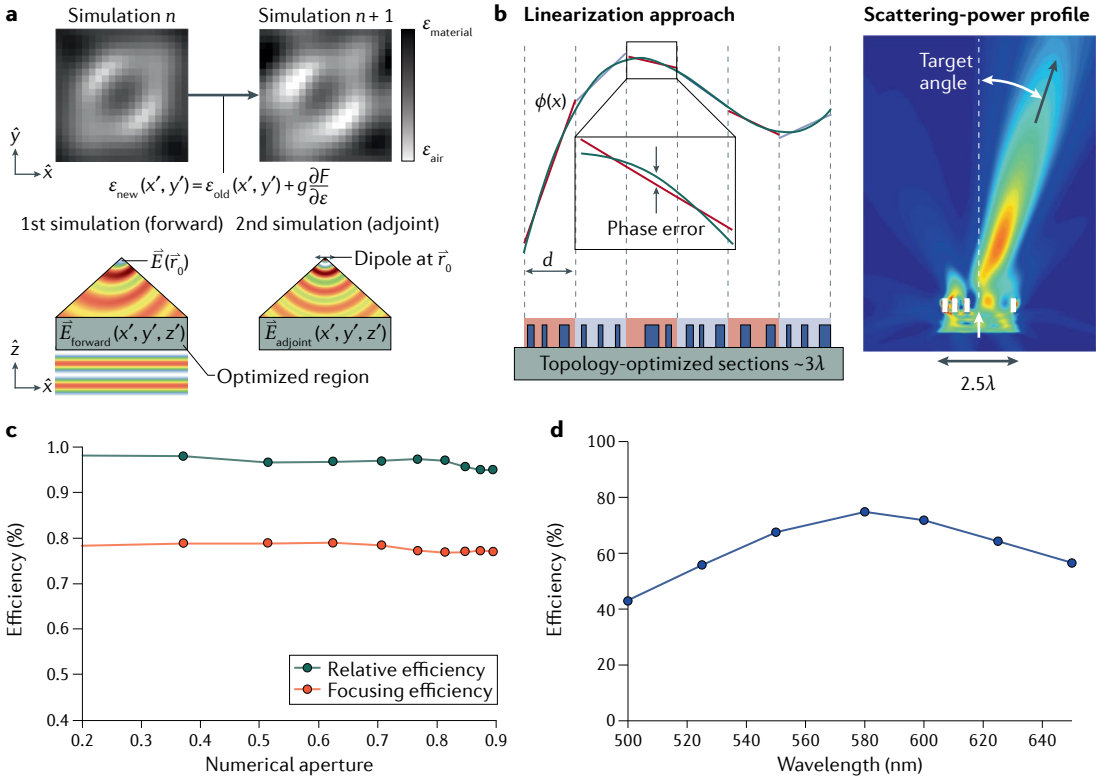

Fig. 3 | **Topology optimization and local approximation for designing large metalenses. a** | Principle of topology optimization. The top view of the distribution of the permittivity ε in the optimization region is shown in the upper part of the panel. The permittivity has an analogue distribution with spatial coordinates and is iteratively changed to optimize the figure of merit F (g is a spatially dependent scalar function). For each iteration, this can be achieved using only two simulations: forward and adjoint, as shown in the lower part of the panel. The new distribution of permittivity ε_{new} is slowly binarized in each iteration, so that it only takes the values of air and of the chosen material; this ensures that the eventual design can be fabricated by a single-step lithographic process. **b** | For the simulation and design of large metalenses, local approximation is used to approximate a continuous phase profile $\phi(x)$ through linear phase segments. The corresponding nanostructures are then designed to scatter light to an angle given by the slope of the linear phase in each segment (right subplot). **c** | A single-crystal silicon metalens designed using both topology-optimization and local-approximation techniques maintains high focusing efficiency (orange curve) of 80% up to a numerical aperture of 0.9. **d** | A TiO_2 metalens designed by local approximation only still has a high focusing efficiency of 75% for a numerical aperture of 0.94. The constituent nanostructures, as shown in the insets, are circular pillars. Panels **b** and **c** adapted from REF.[87], CC BY 4.0. Panel **d** adapted with permission from REF.[88], © The Optical Society.

design single-crystal silicon nanoridges for each section[87]. At λ_d, the relative efficiency of this topology-optimized metalens can be as high as 95% for a high numerical aperture (FIG. 3c), whereas the focusing efficiency is about 80%. A TiO_2 metalens with a high numerical aperture of 0.94 and $\lambda_d = 580$ nm designed using the local approximation but not topology optimization reached a focusing efficiency of 75%[88] (FIG. 3d).

The design of 3D or multilayered metalenses is inherently more computationally costly than the design of their 2D counterparts, but is still tractable with sufficient resources and under proper approximations. A topology-optimized metalens made of TiO_2 designed by 3D full-wave simulations under local approximation is shown in FIG. 4a. Its diameter is about 40 μm. By comparing FIG. 4a and FIG. 2c, one can see that the nanostructures are no longer regular and, instead, exhibit a ring-like pattern with higher density close to the geometrical centre, in order to impart a larger phase delay. FIGURE 4b shows the largest modelled metalens reported to date, with a diameter of 1,200λ (REF.[89]). This metalens is composed of five layers of TiO_2 nanoridges (black rectangles) embedded in a silica matrix and can focus monochromatic incident light of different angles to the same position, as shown on the colour map. The averaged relative efficiency over the design angles is about 55%. Note that the efficiency of such metalenses has a theoretical limit based on reciprocity and brightness theorems[90].

To realize simulations more accurate than those based on local approximation, an overlapping-domain approximation that considers the interaction of neighbouring sections for better accuracy was proposed[91]. Another method to consider the interaction between each section was also introduced[92]. The first approach was used to fabricate a topology-optimized achromatic 2D metalens (metalens diameter 200λ, numerical aperture 0.71) with an averaged focusing efficiency of about 50%[91]. This metalens consists of 15 gradient-index layers with refractive index ranging from 1.5 to 2.4, each 150 nm thick. Such an achromatic metalens is difficult to fabricate, and a more practical design was recently

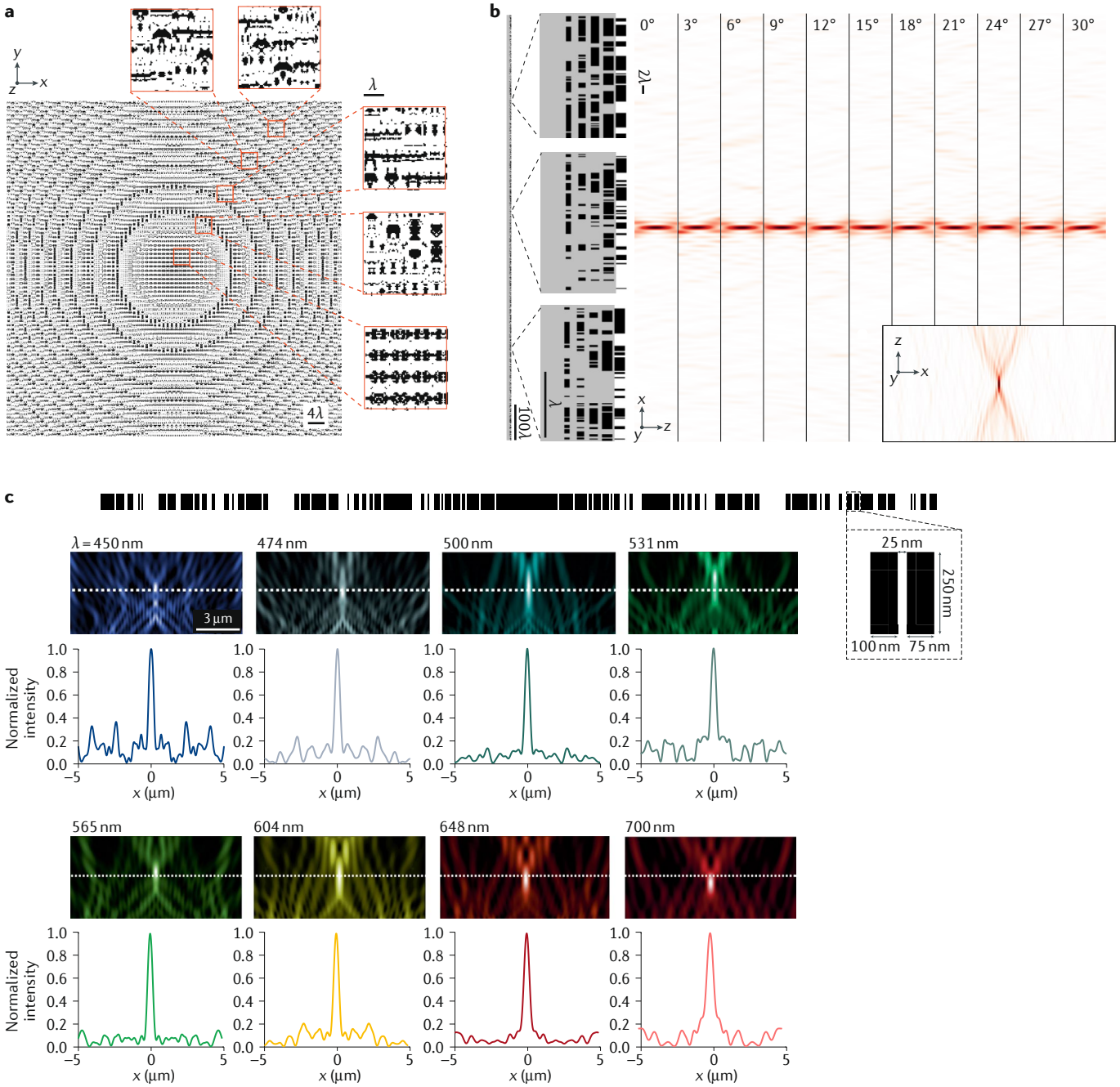

Fig. 4 | **Metalenses designed by topology optimization. a** | A topology-optimized metalens consisting of free-form nanostructures, more complicated than those in FIG. 2c. Designing such a metalens is time-consuming because it involves solving Maxwell equations in three spatial dimensions. **b** | A large (approximately a millimetre in diameter), five-layered metalens focusing incident light of different angles of incidence (indicated on top of the colour map showing the simulated focusing) to the same point. **c** | Achromatic topology-optimized 2D metalens comprising a single layer of TiO_2 nanostructures. The insets show simulated focal spots of different wavelengths being focused on the same plane. Panels **a** and **b** adapted with permission from REF.[89], © The Optical Society. Panel **c** adapted with permission from REF.[93], © The Optical Society.

proposed[93] (FIG. 4c). The resulting achromatic cylindrical metalens was designed without either local or overlapping approximations, owing to its relatively small size of 12.5 μm. The metalens has a numerical aperture of 0.9 and a peak focusing efficiency of about 30% at $\lambda = 680$ nm. However, for wavelengths not specified in the objective function in topology optimization, the efficiency drops quickly.

Broadband achromatic metalenses

If one repeats the ray-tracing process delineated in Eq. 1 for various incident wavelengths, the target-phase profile to achromatically focus broadband incident light must fulfil the relationship:

$$\Phi(r,\omega) = -\frac{\omega}{c}\left(\sqrt{r^2+f^2} - f\right) \quad (5)$$

where ω is the angular frequency of incident light and c the speed of light in vacuum, and the focal length f is a constant[94]. This phase profile is not only a function of the spatial coordinate r but also of frequency. This means that the metalens exhibits different phase profiles depending on the wavelength of incident light. The Taylor expansion of Eq. 5 gives:

$$\Phi(r,\omega) = \Phi(r,\omega_d) + \left.\frac{\partial\Phi}{\partial\omega}\right|_{\omega_d}(\omega-\omega_d) + \left.\frac{\partial^2\Phi}{2\partial\omega^2}\right|_{\omega_d}(\omega-\omega_d)^2 + O(\omega^3). \quad (6)$$

The first term on the right-hand side is the same as in Eq. 1 and leads to a spherical transmitted wavefront[67,95]. The design frequency ω_d is usually chosen at the centre of a bandwidth of interest. The first-order and second-order derivative terms are the group delay and group-delay-dispersion profile, respectively, which control the chromatic focal-length shift of the metalens. The more derivative terms one considers, the better the correction of chromatic focal-length shift. In other words, a nanostructure placed at a coordinate r should ideally fulfil the phase, group delay and group-delay-dispersion requirements simultaneously. An intuitive physical picture to better understand Eq. 6 is shown in FIG. 5a (REF.[95]). By considering polychromatic incident light as comprising individual wave packets, the role of the nanostructures (depicted by blue rectangles) can be understood to be providing a larger time delay at the centre of the metalens than on the sides, such that a transmitted wave packet from the centre can arrive at the focus at the same time as the peripheral wave packets. The required time delay is given by the group-delay profile: $\frac{\partial\Phi(r,\omega)}{\partial\omega} = -\frac{\left(\sqrt{r^2+f^2}-f\right)}{c}$. The second-order and other high-order derivatives are uniformly zero for all coordinates; this implies that, when wave packets leaving from different coordinates r arrive at the focus, they are identical in the temporal domain. The net effect is to ensure that all transmitted light of different wavelengths constructively interfere at the focus. A similar description of achromatic focusing has been proposed by researchers in the ultra-fast-laser community[96,97]. One can follow the design flow chart shown in FIG. 2 to design an achromatic metalens; however, the constituent nanostructures must be more complicated, because a nanostructure placed at a coordinate has to fulfil multiple conditions of phase, group delay and group-delay dispersion. One possible way to increase the number of degrees of freedom in the design is shown in FIG. 5b: this consists of using coupled nanofins to impart different group delay (the derivative of phase with respect to ω) and group-delay dispersion (the second-order derivative). The gap between the nanofins supports a slot-waveguide mode that leads to better tuning of the phase and dispersion[98,99]. In addition, for anisotropic nanofins, a rotation of 90° imparts a phase change of π without affecting the higher-order dispersion terms, because the latter are based on geometrical parameters, whereas the former is based only on the frequency-independent Pancharatnam–Berry phase. Based on this approach, an achromatic and diffraction-limited metalens (numerical aperture 0.2, diameter 25 μm) in the visible was demonstrated (FIG. 5c), as well as chromatic metalenses with controlled focal-length shift[95]. The inclusion of hollow pillars in the nanostructure library to increase phase compensation was exploited to demonstrate an achromatic GaN metalens for colour images[100] (FIG. 5d). In these two cases, the nanostructures were designed to fulfil the requirements of dispersion, and subsequently rotated to satisfy those of the phase profile (first term of Eq. 6). The rotation is necessary because, for these dielectric nanostructures, the effective index of refraction and effective group index are not equal. Intriguingly, a plasmonic slot-waveguide structure whose effective index of refraction is nearly constant over a large bandwidth was proposed and used to build achromatic metalenses[101] (FIG. 5e). Although such plasmonic metalenses suffer from a strong optical loss and reflection at the interface, the broadband dispersionless effective index of refraction is an attractive property[102,103].

The achromatic metalenses discussed so far are polarization-sensitive; that is, they can only focus a given incident polarization. One way to overcome this limitation is to use isotropic nanostructures with circular or square shapes[104,105] (FIG. 5f,g). Such metalenses were designed for near-infrared wavelengths with an achromatic focusing bandwidth of a few hundreds of nanometres. A metalens in reflection configuration, similar to that shown in FIG. 5g, was demonstrated in the visible for achromatic focusing over a bandwidth of approximately 60 nm centred at $\lambda = 530$ nm (REF.[106]). Alternatively, one can use anisotropic nanofins and limit their orientation, so they are either parallel or perpendicular to each other. A layout of such an achromatic metalens is shown in FIG. 5h (REF.[67]). The use of anisotropic nanostructures expands the nanostructure library and, therefore, ensures a more precise implementation of phase and dispersion profiles.

The group delay achievable with nanostructures is limited because it is fundamentally bounded by the nanostructure's height divided by its group index. For example, the range of group delays that a library of 600-nm-tall TiO_2 nanostructures operating in the visible can cover is approximately 6 femtoseconds. An equation that links the trade-off inherent between numerical aperture, diameter and group delay for diffraction-limited and broadband achromatic metalenses has been derived in REFS[95,104,105]. Further increasing the nanostructures' height results in an increased aspect ratio and causes fabrication challenges. Nevertheless, nanostructures with an aspect ratio larger than 20 have been demonstrated[107] and one can also cascade nanostructured multilayers to naturally increase the range of group delay for wide-field-of-view and achromatic metalenses[41,52,108,109]. Another possibility is to explore the use of hyperbolic metamaterials, which can support propagating modes with very large group index[110,111]. Some key performance metrics related to broadband achromatic metalenses in various frequency regions are summarized in TABLE 1.

Emerging applications

Notwithstanding the limited achievable group delay, one can stitch achromatic metalenses to form a lens array for various applications. An achromatic GaN metalens array for depth sensing was reported[112] (FIG. 6a). The pixellated image of an object, which carries depth information, was formed by a refractive lens and an achromatic metalens array. After post-processing the pixellated image, one can

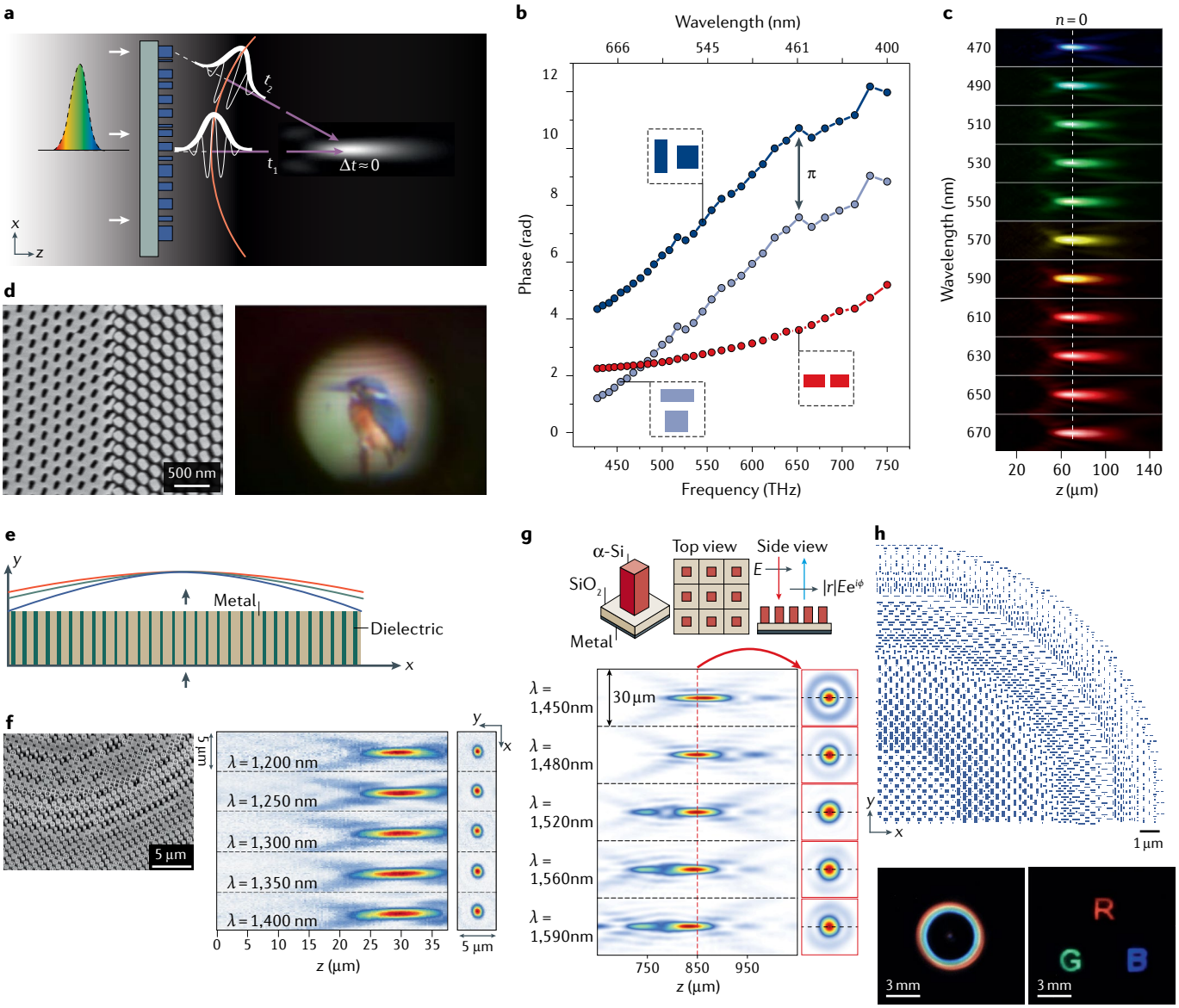

Fig. 5 | **Broadband achromatic metalenses. a** | The achromaticity condition can be interpreted as requiring transmitted wave packets to reach the focus at the same time and maintain an identical temporal profile. **b** | By introducing coupled nanofins in a single unit cell, one can obtain additional degrees of freedom in the design to tune phase and dispersion independently. The group delay (the slope) and group-delay dispersion (the curvature) are tuned by different combinations of nanostructure lengths and widths, whereas slope and curvature can be kept unchanged when adjusting the phase by rotation, as in the case of the dark and light blue nanostructures with a 90° rotation. **c** | Experimental intensity distribution (point-spread functions) of an achromatic metalens in the visible. **d** | Achromatic GaN metalenses used for colour imaging. Additional degrees of freedom were introduced by adding hollow nanostructures to the library. An example of an imaged colour object is shown. **e** | An achromatic metalens comprising plasmonic metal–dielectric waveguides and operating in the near-infrared. The waveguide possesses the interesting property of maintaining a nearly constant effective index of refraction over a large bandwidth. **f–h** | Achromatic and polarization-insensitive metalenses in the near-infrared (panels **f** and **g**) and in the visible (panel **h**). The metalens in panel **f** consists of silicon pillars and rings, shown in the scanning microscope image. The right panel shows focal spots and point-spread functions measured at different wavelengths. The configuration of the metalens in panel **g** is in reflection, with silicon square pillars on a layer of SiO_2 on an aluminium mirror. This increases the optical path and introduces resonances for larger phase and dispersion coverage. The bottom part of the panel shows point-spread functions and focal spots with more severe secondary foci than those seen in panel **f**. Instead of using isotropic nanostructures as shown in panels **f** and **g**, the metalens configuration in panel **h** comprises anisotropic nanofins. The lower part of the panel shows the obtained images of colour objects. Panels **a** and **c** adapted from REF.[95], Springer Nature Limited. Panel **d** adapted from REF.[100], Springer Nature Limited. Panel **e** adapted from REF.[101], CC BY 4.0. Panel **f** adapted from REF.[104], CC BY 4.0. Panel **g** adapted with permission from REF.[105], © The Optical Society. Panel **h** adapted from REF.[67], CC BY 4.0.

Table 1 | **Summary of performance metrics for broadband achromatic metalenses**

Diameter (μm)	NA	Material	Nanostructure height (nm)	Bandwidth (μm)	Peak efficiency	Polarization	Ref.
100	0.24	a-Si	800	1.3–1.66	55% (measurement)	Insensitive	104
26	0.2	TiO_2	600	0.46–0.7	36% (measurement)	Insensitive	67
30	0.35	GaAs	2,000	3–4	52% (measurement)	Insensitive	173
200	0.2	TiO_2/SiO_2/Al mirror	600/180/110	0.49–0.55	20% (measurement)	Insensitive	106
240	0.18	a-Si/SiO_2/Al mirror	725/325/100	1.45–1.59	55% (measurement)	Insensitive	105
14	0.08	Si_3N_4	400	0.43–0.78	55% (measurement)	Insensitive	114
7	0.17	Polymer	400	0.435–0.685	20% (measurement)	Insensitive	174
50	0.1	GaN	800	0.4–0.64	67% (measurement)	Circular	100
220	0.02	TiO_2	600	0.47–0.67	20% (measurement)	Circular	95
56	0.27	Au/SiO_2/Au mirror	30/60/150	1.2–1.65	13% (measurement)	Circular	175
77	0.8	Si	4,000	3.7–4.5	20% (simulation)	Circular	176
200	0.46	Au/MgF_2/Si/Au mirror	200/800/200/~400	8–12	63% (simulation)	Circular	177
64	0.81	Si	800	1.47–1.59	27% (simulation)	Circular	178
38	0.3	Si	1,000	1–1.2	45% (simulation)	Circular	179
22	0.21	GaN	800	0.4–0.66	75% (simulation)	Circular	112
~100	0.7	TiO_2	3,150	0.48–0.7	>50% (simulation)	Linear	89
12.5	0.1	TiO_2	250	0.45–0.7	80% (simulation)	Linear	93
12.5	0.9	TiO_2	250	0.45–0.7	33% (simulation)	Linear	93
~10	0.7	Au	3,000	1–2	Not reported	Linear	101

The polarization sensitivity specifies what incident polarization can be focused. NA, numerical aperture.

reconstruct and selectively focus different parts of the image, obtaining their depth (FIG. 6b). Interestingly, the reverse process can also be utilized to project 3D images to the far field. This technique is referred to as integral imaging[113]. This concept was demonstrated using an array of achromatic SiN metalenses[114] (FIG. 6c). Also, different patterned metal films were used to project images of the characters '3' and 'D' with different depths (FIG. 6d). This type of work provides a solution to the accommodation–vergence conflict present in virtual-reality or argument-reality devices, which arises because the brain receives mismatching cues about the distance of a 3D object and the focusing distance required to focus on it[115,116].

As previously mentioned, metalenses can be customized to provide aspherical phase and dispersion (including group delay and group-delay dispersion) profiles, which can be used to eliminate monochromatic (such as spherical, coma, astigmatism) and chromatic aberrations. A metacorrector to eliminate the aberrations of a singlet refractive lens was demonstrated[117] (FIG. 6e). This type of metasurface-refractive hybrid lens is conceptually more advanced than conventional diffractive-refractive lenses[118] because the group-delay dispersion is taken into account, resulting in a better correction of the chromatic focal-length shift (see the supplementary figure S1 of REF.[117]). For standard USAF resolution charts illuminated by incoherent white light, utilizing the metacorrector together with the lens substantially reduces the blurring of the image and the colour spread. By using the same design approach, a metacorrector can eliminate residual aberrations in a high-numerical-aperture oil-immersion objective[117]. Note that the air gap between the metacorrector and the refractive lens is not a crucial parameter. One can attach the metacorrector on the planar side of the refractive lens so that the overall device is still a single element. A combination of a refractive prism and a metasurface as an achromatic hybrid element has been developed[119] (FIG. 6f). The deflection angles of wavelengths have been measured by Fourier microscopy[120,121]: the upper line in FIG. 6f results from the first-order diffraction of the metasurface and is more horizontal compared with the lower line (the zeroth order, which does not interact with the metasurface). This indicates that the deflection angle is almost identical for various incident wavelengths.

Another interesting direction arises from the fact that dispersion-engineered metalenses allow one to control the spatial location of the focal spot for each incident wavelength. One can, therefore, realize a dispersion-engineered chromatic metalens for spectroscopic applications. Conventional grating-based spectrographs, similar to imaging lenses, suffer from numerous types of aberrations, resulting in low spectral resolution and a limited bandwidth. Off-axis-focusing metalenses combine both focusing and dispersive functions in a single device and can efficiently send light to larger angles than conventional gratings, because they do not suffer from drawbacks such as shadowing effects. This results in a substantially improved dispersion that leads to a higher spectral resolution[56,57,122,123]. However, such off-axis-focusing metalenses usually suffer from various aberrations, particularly astigmatism and field curvature, which results in enlarged and blurry focal spots when projecting onto a camera. This limits the bandwidth of operation (FIG. 7a, upper panel). With dispersion engineering, one can adjust the location of

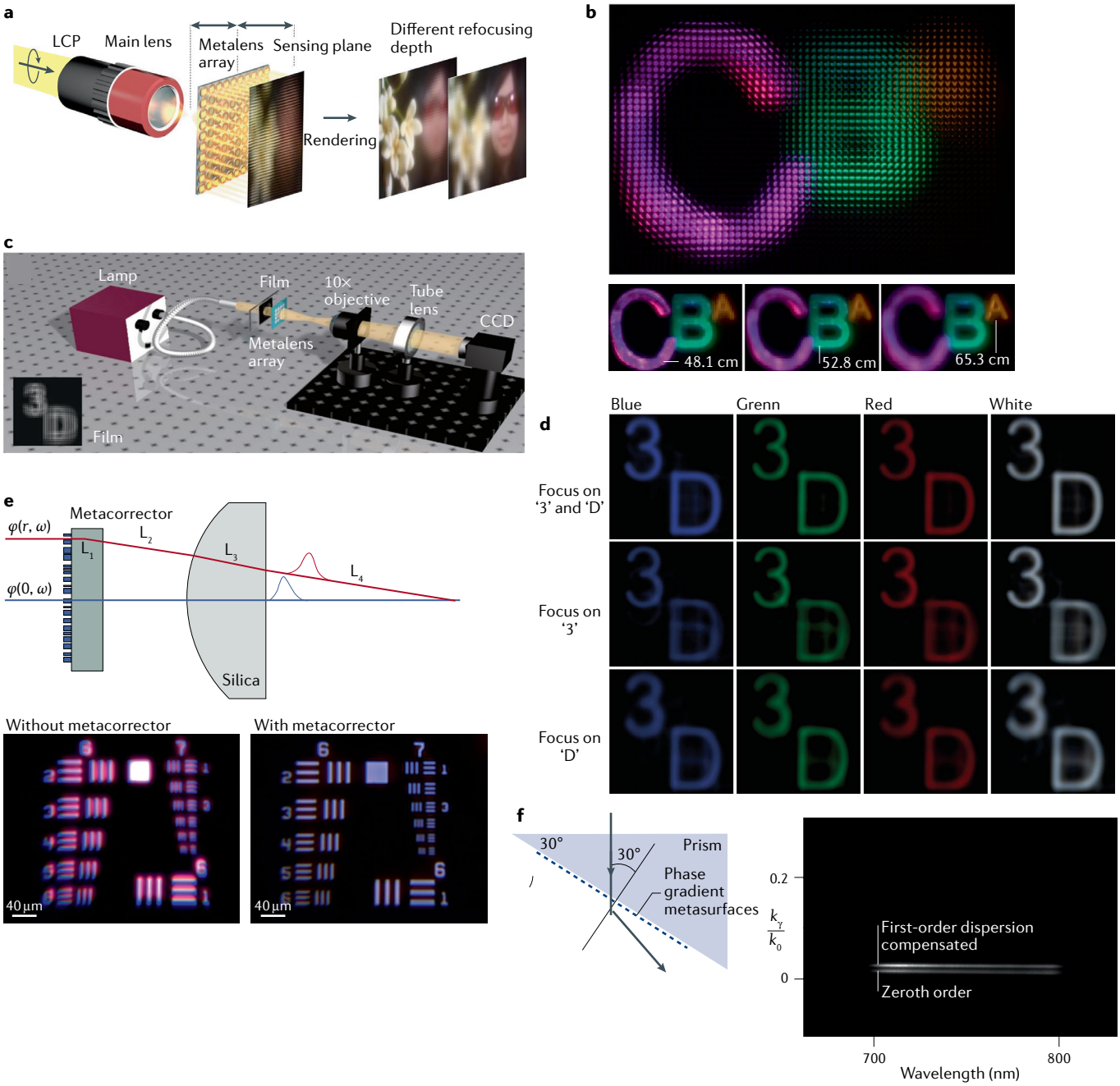

Fig. 6 | **Dispersion-engineered metasurfaces and metalenses. a** | A depth-sensing and imaging system consisting of a microscope objective and an achromatic GaN metalens array can resolve multiple images at different depths. **b** | Three letters of different colours are imaged at various depths. The top panel shows the original image captured by the GaN metalens array on a colour camera. After image processing, one can selectively view the letters 'C', 'B' or 'A' in focus, and their depths can be determined. **c** | The reverse of the process illustrated in panel **a** consists of projecting various images across different wavelengths to different depths in the far field to obtain a 3D image using an achromatic SiN metalens array. **d** | In this example, each row corresponds to a different patterned metal film that projects the characters '3' and 'D' to different focal planes. For example, in the middle row, the '3' is focused and the 'D' is blurred because it was focused to a further depth. The chromatic aberration of this system is well corrected, as no significant blurriness is observed under illumination from blue to red wavelengths. **e** | Metasurfaces can also be used as aberration correctors (metacorrectors) that work in conjunction with low-cost, refractive singlet lenses to eliminate chromaticity. The metacorrector was designed such that all incident rays (following paths from L1 to L4) reach the focus with the same values of phase, group delay and group-delay dispersion as the chief ray, which is the ray passing through the lens centre (blue). The bottom pictures show a comparison of imaging performance under the same illumination, with and without the metacorrector. **f** | A corrective metasurface can also be integrated on the side of a glass prism to suppress dispersion. Measurements from a Fourier microscope show two lines, corresponding to the zeroth-order and first-order transmitted light from the device. The correction of the prism dispersion can be observed from the slopes of the lines. k_y/k_0 is the magnitude of normalized transverse wavevector. CCD, charge-coupled device; LCP, left-handed circularly polarized light. Panels **a** and **b** adapted from REF.[112], Springer Nature Limited. Panels **c** and **d** adapted from REF.[114], CC BY 4.0. Panel **e** adapted with permission from REF.[117], ACS. Panel **f** adapted with permission from REF.[119], Wiley-VCH.

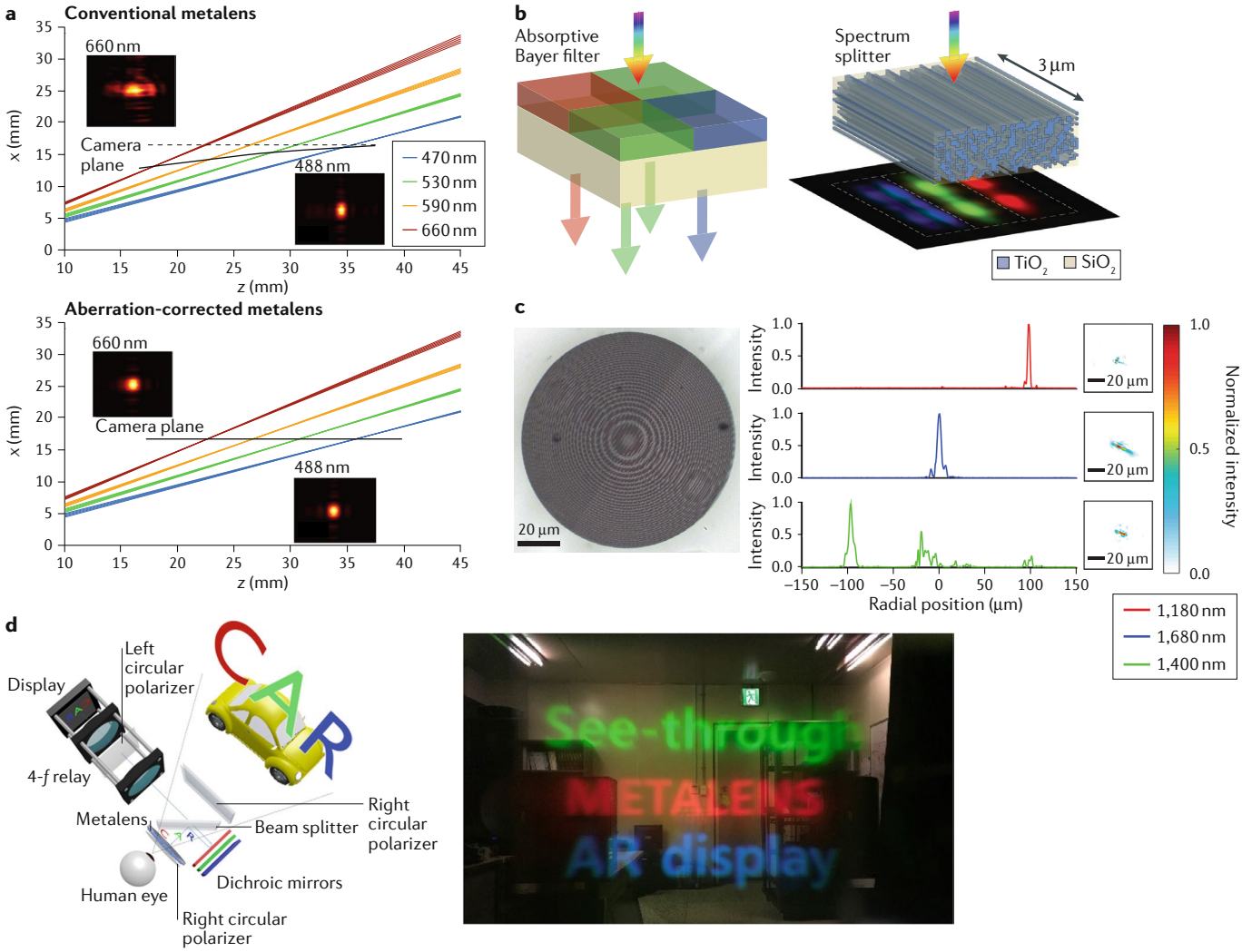

Fig. 7 | **Applications of metalenses with designed chromatic dispersion. a** | A dispersion-engineered, off-axis metalens can be used to realize an aberration-corrected spectrometer, in which the chromatic-induced broadening of the focal spot and field curvature are suppressed. In a conventional metalens, these problems result in limited bandwidth and resolution. **b** | Metalenses could potentially replace conventional Bayer filters by sorting different colours (within a specified bandwidth) to different spatial locations. The metalens shown on the right comprises TiO_2 nanostructures in a SiO_2 matrix, and could potentially improve efficiency, as no spatial multiplexing of the device is necessary. **c** | A metalens akin to that proposed in panel **b**, focusing three near-infrared wavelengths at three different spatial locations, is shown. The right part of the panel shows the measured intensity distributions and focal spot profiles for the three wavelengths. **d** | A virtual-reality and augmented-reality device based on a metalens with a large field of view. The metalens is used in conjunction with various traditional optical components, such as dichroic mirrors, located at different planes to achromatically project a virtual coloured image accurately to the human eye. The picture on the right shows that the view of the surrounding real objects is not obstructed. Panel **a** adapted with permission from REF.[55], Wiley-VCH. Panel **b** adapted with permission from REF.[127], © The Optical Society. Panel **c** adapted with permission from REF.[128], ACS. Panel **d** adapted from REF.[129], CC BY 4.0.

focal spots at various wavelengths such that they are tightly focused on the flat camera plane with negligible aberrations within a certain bandwidth[56] (which can include most of the visible spectrum; FIG. 7a, lower panel). It is also possible to pattern off-axis metalenses to increase the field of view for imaging spectrometers[53,54] or spectropolarimeters[124–126].

Another possible application relies on focusing different incident wavelengths, red, green and blue, with a given bandwidth to three distinct spots. Such a metalens could potentially replace the Bayer colour filters widely used in colour cameras. This is promising because conventional Bayer filters are spatially multiplexed into four subpixels (usually arranged in a two-by-two matrix with two green filters and one blue and one red filter) and only allow the bandwidth of interest to pass through (FIG. 7b). This spatial multiplexing caps the maximum efficiency at 25% for each subpixel. Metalenses can, in principle, circumvent this constraint by using a colour-sorting instead of a filtering approach. A design of such a metasurface comprising complicated TiO_2 nanostructures in SiO_2 matrix was numerically proposed

(FIG. 7b) to sort three primary colours to different spatial positions[127]. An experimental demonstration of this concept in the near-infrared, based on a two-layer a-Si metasurface, is shown in FIG. 7c (REF.[128]). Finally, the metalens in FIG. 7d is not dispersion engineered, but the researchers placed dichroic mirrors at different planes along the optical axis to mitigate chromatic aberration[129]. The metalens has a large diameter of 2 cm and was manufactured by nanoimprint. It can be situated close to the human eye to provide a large field of view for applications in virtual and augmented reality. Other methods to circumvent chromatic aberration are based on Moiré lenses[130], computational processing[131] and the design of metalenses with tunable focal length for different incident polarizations[132,133]. In the latter case, by a proper control of incident polarization of each wavelength, the metalens can achieve achromatic focusing in the visible.

Perspectives

Metasurface research has progressed tremendously in the past few years, with key developments in both theoretical modelling and nanofabrication techniques that have been applied to an increasingly varied range of materials. Initial results are promising, particularly with regards to the reduction in form factor and system complexity for many sophisticated optical systems. For example, metalenses enabled a snapshot full-Stokes polarization camera with minimal optical components and no moving parts[134], compact and high-resolution microscopes[135,136] and depth-sensing cameras based on multi-focal-length metalenses[137,138]. In essence, metasurfaces represent an opportunity for two industries, semiconductor manufacturing and lens making and assembly, to potentially work in unison for disruptive innovation. The same technology for fabricating computer and sensor chips can be used for metalenses and other metasurface components. This will lead to foundries that will manufacture cameras based on the integration of flat optics and complementary metal–oxide–semiconductor (CMOS) technology[139]. It is no surprise then, that metalens technology was chosen by the World Economic Forum and Scientific American as one of the top ten emerging technologies of 2019. Additionally, Lux Research forecasted that the metamaterials and metasurfaces industry might have a market size of up to US $10 billion by 2030 and the Defense Advanced Research Projects Agency (DARPA) of the United States started an extreme-optics programme to develop revolutionary optical components. However, multiple challenges, both theoretical and experimental, still have to be overcome for continued development. We believe that, at this stage in metasurface research, it is important to explore possible solutions to address the size limitation in achromatic metalenses. As noted in an earlier section, this limitation is fundamentally due to current fabrication limitations in realizing high-aspect-ratio nanostructures and stacking multiple layers of metasurfaces. This places an upper bound on the maximum dispersion that can be achieved for a given nanostructure and, therefore, limits the overall size of the device. Another way forward is to strike a compromise by designing a metalens that can achromatically focus multiple discrete wavelengths, akin to conventional multi-order diffractive lenses[140,141]. In this case, the metalens diameter could increase substantially to the centimetre scale. Intriguingly, such multi-wavelength achromatic focusing metalenses have been demonstrated[94,142,143] long before the realization of continuous achromatic broadband metalenses; however, it remains to be seen what is the optimal configuration in terms of the largest achievable diameter, number of achromatically focused wavelengths and numerical aperture in such metalenses.

On the manufacturing and processing side, in order to achieve widespread integration of metasurface components into everyday electronic products, the fabrication process must be compatible with existing low-cost, large-scale foundry technology, such as deep-ultraviolet projection lithography[144–146] and roll-to-roll nanoimprint[147,148]. Although there have been a few reports on metasurfaces made by deep-ultraviolet projection lithography in the near-infrared wavelengths, it is challenging to manufacture metasurface components in the visible range (particularly the shorter wavelengths) with high efficiency due to resolution limitations. A related fabrication strategy that would be greatly interesting to develop is the fabrication of metasurfaces on curved substrates: these provide substantial advantages in eliminating higher-order Seidel aberrations[149]. Possible ways to realize this strategy include transfer-based processes in which the metasurface is patterned onto a flexible polymer[150,151] and the direct use of lithographic techniques on a curved substrate[152,153].

From a software perspective, the design of metasurface components typically involves a host of different programs employing ray tracing, wave optics and full-wave Maxwell equation solvers, as well as customized codes for post-processing. Obvious drawbacks of using different software programs are the difficulties and inefficiencies related to data transfer, as well as the substantial time overhead needed to learn and master each individual program. Some particularly astute companies have noticed this and are working to provide their solutions. For instance, Zemax has teamed up with Lumerical to introduce functions that directly import finite-difference time-domain simulated results into ray-tracing solvers; Synopsys has combined their products CODE V and RSoft for metalens design; LightTrans has developed a package for metalens design based on wave optics; and the start-up company PlanOpSim is developing a metasurface design software with an all-in-one graphical user interface. We believe that another useful feature to incorporate into these software packages is topology optimization. In particular, the incorporation of artificial intelligence and machine-learning techniques would be extremely helpful[154–156], as current outputs of topology optimization are often trapped in a local minimum due to the sheer number of parameters involved. Because this number naturally scales with the size of the metasurface device being designed, this would go a long way towards enabling larger, more sophisticated meta elements. The training process of machine learning requires a huge data set to train the neural network. Fan's group at Stanford University is working with others to set up a database called Metanet, in which one can find many

topology-optimized metasurfaces to be used as training data, as well as preliminary source codes.

Last but not least, along with REF.[157], we would like to address the difference between metalenses and conventional Fresnel lenses. As we discussed, in addition to the control of polarization, metalenses can also impart independent phase and dispersion profiles to control chromatic focal-length shift. Recently, a research article from Zeiss[158] pointed out that conventional saw-tooth Fresnel lenses suffer rapid efficiency drop with increasing angle of incidence because of shadow effect leading to significant vignetting. This drawback also exists in recently developed multilevel diffractive lenses[159,160] and is intrinsic to such designs: the shadowing effect is a direct result of controlling phase delay by varying heights. In addition, the spherical aberrations in experimentally realized multilevel diffractive lenses are usually severe, resulting in a low Strehl ratio[160,161], which is a number between 0 and 1 that describes how close an experimentally measured focal-spot profile is to an ideal Airy disk. Note that claiming a lens (no matter what type) is diffraction limited only based on the full-width at half-maximum of the focal spot is not appropriate. The Strehl ratio is a more essential factor. Finally, the constituent nanostructures of metalenses are inorganic and have a high index of refraction, whereas those of multilevel diffractive lenses are usually polymer based. This makes metalenses more suitable in harsh environments and easier to integrate with other optical devices, such as vertical-cavity surface-emitting lasers[162,163], spatial light modulators[164] and large-angle beam deflectors for lidars[165].

This Review is focused on dispersion-engineered metalenses; other reviews are available on flat-optics applications on lidars, radiative cooling, broadband polarizers and filters and nanolithography[166–170], and active metasurfaces[171,172]. In summary, we have explored the role of metasurfaces in modern far-field optical systems, particularly achromatic ones, in which metasurfaces have a particular edge over conventional optical elements due to the possibility to freely engineering the effective index of refraction by varying geometrical parameters. This allows one to break free from traditional material constraints, so long as the constituent material of the nanostructures possesses a sufficiently high index of refraction and has low loss. Depending on the intended wavelength of operation, viable material candidates include various high-index dielectrics, III–V semiconductors and different phases of silicon. We have provided the basic physical picture behind the interaction of light with generic dielectric nanostructures and have showed how the imparted phase and its higher-order derivatives can be physically understood. We have also illustrated how a suitable metasurface can be obtained with various simulation techniques, such as ray tracing and the use of free-form shapes derived from advanced modelling methods like topological optimization. Although achromatic focusing for imaging systems is arguably the most direct and important application of dispersion-engineered metasurfaces, they are also viable candidates in areas such as augmented and virtual reality, as well as colour filters for various electronic sensors and displays. We believe that the continued growth of flat-optics technology hinges on advances in modelling techniques in which ray tracing, wave optics and finite-element methods should be integrated seamlessly, and on the development of a reliable, large-scale, low-cost manufacturing process. Major steps have already been taken in this direction, and the future of metasurfaces is promising as academics and industry increasingly put resources towards this nascent technology; for example, a new centre for meta-optical systems supported by the Australian Research Council has opened for developing essential optical technologies for industry 4.0: the fourth industrial revolution, an incubator meeting of flat optics held by the Optical Society identified promising research topics and research programmes are being funded by Samsung and Sony.

Published online: 19 June 2020

1. Grüner-Nielsen, L. et al. Dispersion-compensating fibers. *J. Lightwave Technol.* **23**, 3566–3579 (2005).
2. Smith, G. H., Novak, D. & Ahmed, Z. Overcoming chromatic-dispersion effects in fiber-wireless systems incorporating external modulators. *IEEE Trans. Microw. Theory Tech.* **45**, 1410–1415 (1997).
3. Brabec, T. & Krausz, F. Intense few-cycle laser fields: frontiers of nonlinear optics. *Rev. Mod. Phys.* **72**, 545 (2000).
4. Weiner, A. M. Femtosecond pulse shaping using spatial light modulators. *Rev. Sci. Instrum.* **71**, 1929–1960 (2000).
5. Strickland, D. & Mourou, G. Compression of amplified chirped optical pulses. *Opt. Commun.* **55**, 447–449 (1985).
6. Herzberger, M. & McClure, N. R. The design of superachromatic lenses. *Appl. Opt.* **2**, 553–560 (1963).
7. Newton, I. A new theory about light and colors. *Am. J. Phys.* **61**, 108–112 (1993).
8. Hartmann, P. *Optical Glass* (SPIE, 2014).
9. Hartmann, P., Jedamzik, R., Reichel, S. & Schreder, B. Optical glass and glass ceramic historical aspects and recent developments: a Schott view. *Appl. Opt.* **49**, D157–D176 (2010).
10. Voelkel, R. Wafer-scale micro-optics fabrication. *Adv. Opt. Technol.* **1**, 135–150 (2012).
11. Khorasaninejad, M. & Capasso, F. Metalenses: versatile multifunctional photonic components. *Science* **358**, eaam8100 (2017).
12. Lalanne, P. & Chavel, P. Metalenses at visible wavelengths: past, present, perspectives. *Laser Photonics Rev.* **11**, 1600295 (2017).
13. Li, B., Piyawattanametha, W. & Qiu, Z. Metalens-based miniaturized optical systems. *Micromachines* **10**, 310 (2019).
14. Mueller, J. P. B., Rubin, N. A., Devlin, R. C., Groever, B. & Capasso, F. Metasurface polarization optics: independent phase control of arbitrary orthogonal states of polarization. *Phys. Rev. Lett.* **118**, 113901 (2017).
15. Arbabi, A., Horie, Y., Bagheri, M. & Faraon, A. Dielectric metasurfaces for complete control of phase and polarization with subwavelength spatial resolution and high transmission. *Nat. Nanotechnol.* **10**, 937–943 (2015).
16. Ding, F., Wang, Z., He, S., Shalaev, V. M. & Kildishev, A. V. Broadband high-efficiency half-wave plate: a supercell-based plasmonic metasurface approach. *ACS Nano* **9**, 4111–4119 (2015).
17. Kildishev, A. V., Boltasseva, A. & Shalaev, V. M. Planar photonics with metasurfaces. *Science* **339**, 1232009 (2013).
18. Yu, N. et al. Light propagation with phase discontinuities: generalized laws of reflection and refraction. *Science* **334**, 333–337 (2011).
19. Sun, S. et al. Gradient-index meta-surfaces as a bridge linking propagating waves and surface waves. *Nat. Mater.* **11**, 426–431 (2012).
20. Sun, S. et al. High-efficiency broadband anomalous reflection by gradient meta-surfaces. *Nano Lett.* **12**, 6223–6229 (2012).
21. Devlin, R. C., Khorasaninejad, M., Chen, W. T., Oh, J. & Capasso, F. Broadband high-efficiency dielectric metasurfaces for the visible spectrum. *Proc. Natl Acad. Sci. USA* **113**, 10473–10478 (2016).
22. Liang, Y. et al. High-efficiency, near-diffraction limited, dielectric metasurface lenses based on crystalline titanium dioxide at visible wavelengths. *Nanomaterials* **8**, 288 (2018).
23. Brière, G. et al. An etching-free approach toward large-scale light-emitting metasurfaces. *Adv. Opt. Mater.* **7**, 1801271 (2019).
24. Chen, B. H. et al. GaN metalens for pixel-level full-color routing at visible light. *Nano Lett.* **17**, 6345–6352 (2017).
25. Sell, D., Yang, J., Doshay, S., Zhang, K. & Fan, J. A. Visible light metasurfaces based on single-crystal silicon. *ACS Photonics* **3**, 1919–1925 (2016).
26. Zhou, Z. et al. Efficient silicon metasurfaces for visible light. *ACS Photonics* **4**, 544–551 (2017).
27. Wang, B. et al. Visible-frequency dielectric metasurfaces for multiwavelength achromatic and highly dispersive holograms. *Nano Lett.* **16**, 5235–5240 (2016).
28. Ye, M., Peng, Y. & Yi, Y. S. Silicon-rich silicon nitride thin films for subwavelength grating metalens. *Opt. Mater. Express* **9**, 1200–1207 (2019).
29. Zhan, A. et al. Low-contrast dielectric metasurface optics. *ACS Photonics* **3**, 209–214 (2016).
30. Khorasaninejad, M. et al. Metalenses at visible wavelengths: diffraction-limited focusing and subwavelength resolution imaging. *Science* **352**, 1190–1194 (2016).

31. Iyer, P. P. et al. Unidirectional luminescence from quantum well metasurfaces. Preprint at *arXiv* https://arxiv.org/abs/1905.01816v1 (2019).
32. Li, Q. et al. Single-mode GaN nanowire lasers. *Opt. Express* **20**, 17873–17879 (2012).
33. Li, C. et al. Nonpolar InGaN/GaN core–shell single nanowire lasers. *Nano Lett.* **17**, 1049–1055 (2017).
34. Liang, H. et al. Ultrahigh numerical aperture metalens at visible wavelengths. *Nano Lett.* **18**, 4460–4466 (2018).
35. Chen, W. T. et al. Immersion meta-lenses at visible wavelengths for nanoscale imaging. *Nano Lett.* **17**, 3188–3194 (2017).
36. He, D. et al. Polarization-insensitive meta-lens doublet with large view field in the ultraviolet region. *Proc. SPIE Int. Symp. Adv. Opt. Manufact. Testing Technol.* https://doi.org/10.1117/12.2505584 (2019).
37. Deng, Y. et al. All-silicon broadband ultraviolet metasurfaces. *Adv. Mater.* **30**, 1802632 (2018).
38. Ollanik, A. J., Smith, J. A., Belue, M. J. & Escarra, M. D. High-efficiency all-dielectric Huygens metasurfaces from the ultraviolet to the infrared. *ACS Photonics* **5**, 1351–1358 (2018).
39. Zhang, C. et al. Low-loss metasurface optics down to the deep ultraviolet region. *Light Sci. Appl.* **9**, 55 (2020).
40. Engelberg, J. et al. Near-IR wide-field-of-view Huygens metalens for outdoor imaging applications. *Nanophotonics* **9**, 361–370 (2020).
41. Arbabi, A. et al. Miniature optical planar camera based on a wide-angle metasurface doublet corrected for monochromatic aberrations. *Nat. Commun.* **7**, 13682 (2016).
42. Vo, S. et al. Sub-wavelength grating lenses with a twist. *IEEE Photonics Technol. Lett.* **26**, 1375–1378 (2014).
43. Arbabi, A., Horie, Y., Ball, A. J., Bagheri, M. & Faraon, A. Subwavelength-thick lenses with high numerical apertures and large efficiency based on high-contrast transmitarrays. *Nat. Commun.* **6**, 7069 (2015).
44. Fan, Q. et al. A high numerical aperture, polarization-insensitive metalens for long-wavelength infrared imaging. *Appl. Phys. Lett.* **113**, 201104 (2018).
45. Zuo, H. et al. High-efficiency all-dielectric metalenses for mid-infrared imaging. *Adv. Opt. Mater.* **5**, 1700585 (2017).
46. Yan, C. et al. Midinfrared real-time polarization imaging with all-dielectric metasurfaces. *Appl. Phys. Lett.* **114**, 161904 (2019).
47. Zhang, L. et al. Ultra-thin high-efficiency mid-infrared transmissive Huygens meta-optics. *Nat. Commun.* **9**, 1481 (2018).
48. Shalaginov, M. Y. et al. A single-layer panoramic metalens with >170° diffraction-limited field of view. Preprint at *arXiv* https://arxiv.org/abs/1908.03626 (2019).
49. Aieta, F. et al. Aberration-free ultrathin flat lenses and axicons at telecom wavelengths based on plasmonic metasurfaces. *Nano Lett.* **12**, 4932–4936 (2012).
50. Aieta, F., Genevet, P., Kats, M. & Capasso, F. Aberrations of flat lenses and aplanatic metasurfaces. *Opt. Express* **21**, 31530–31539 (2013).
51. Liang, H. et al. High performance metalenses: numerical aperture, aberrations, chromaticity, and trade-offs. *Optica* **6**, 1461–1470 (2019).
52. Groever, B., Chen, W. T. & Capasso, F. Meta-lens doublet in the visible region. *Nano Lett.* **17**, 4902–4907 (2017).
53. Faraji-Dana, M. et al. Compact folded metasurface spectrometer. *Nat. Commun.* **9**, 4196 (2018).
54. Faraji-Dana, M. et al. Hyperspectral imager with folded metasurface optics. *ACS Photonics* **6**, 2161–2167 (2019).
55. Zhu, A. Y. et al. Compact aberration-corrected spectrometers in the visible using dispersion-tailored metasurfaces. *Adv. Opt. Mater.* **7**, 1801144 (2019).
56. Zhu, A. Y. et al. Ultra-compact visible chiral spectrometer with meta-lenses. *APL Photonics* **2**, 036103 (2017).
57. Khorasaninejad, M., Chen, W. T., Oh, J. & Capasso, F. Super-dispersive off-axis meta-lenses for compact high resolution spectroscopy. *Nano Lett.* **16**, 3732–3737 (2016).
58. Nikolova, L. & Ramanujam, P. S. *Polarization Holography* (Cambridge Univ. Press, 2009).
59. Pancharatnam, S. Generalized theory of interference, and its applications. *Proc. Indian Acad. Sci. Sect. A* **44**, 247–262 (1956).
60. Gori, F. Measuring Stokes parameters by means of a polarization grating. *Opt. Lett.* **24**, 584–586 (1999).
61. Bomzon, Z., Biener, G., Kleiner, V. & Hasman, E. Space-variant Pancharatnam–Berry phase optical elements with computer-generated subwavelength gratings. *Opt. Lett.* **27**, 1141–1143 (2002).
62. Escuti, M. J., Kim, J. & Kudenov, M. W. Controlling light with geometric-phase holograms. *Opt. Photonics News* **27**, 22–29 (2016).
63. Kikuta, H., Ohira, Y. & Iwata, K. Achromatic quarter-wave plates using the dispersion of form birefringence. *Appl. Opt.* **36**, 1566–1572 (1997).
64. Zhao, Y., Belkin, M. A. & Alù, A. Twisted optical metamaterials for planarized ultrathin broadband circular polarizers. *Nat. Commun.* **3**, 870 (2012).
65. Pu, M. et al. Catenary optics for achromatic generation of perfect optical angular momentum. *Sci. Adv.* **1**, e1500396 (2015).
66. Wang, D. et al. Broadband high-efficiency chiral splitters and holograms from dielectric nanoarc metasurfaces. *Small* **15**, 1900483 (2019).
67. Chen, W. T., Zhu, A. Y., Sisler, J., Bharwani, Z. & Capasso, F. A broadband achromatic polarization-insensitive metalens consisting of anisotropic nanostructures. *Nat. Commun.* **10**, 355 (2019).
68. Yoon, G., Lee, D., Nam, K. T. & Rho, J. Geometric metasurface enabling polarization independent beam splitting. *Sci. Rep.* **8**, 9468 (2018).
69. Zhang, X. et al. Polarization-independent broadband meta-holograms via polarization-dependent nanoholes. *Nanoscale* **10**, 9304–9310 (2018).
70. Zhan, T., Xiong, J., Lee, Y.-H. & Wu, S.-T. Polarization-independent Pancharatnam-Berry phase lens system. *Opt. Express* **26**, 35026–35033 (2018).
71. She, A., Zhang, S., Shian, S., Clarke, D. R. & Capasso, F. Large area metalenses: design, characterization, and mass manufacturing. *Opt. Express* **26**, 1573–1585 (2018).
72. Kenney, M. et al. Large area metasurface lenses in the NIR region. *Proc. SPIE Model. Aspects Opt. Metrology VII* https://doi.org/10.1117/12.2527157 (2019).
73. Ra'di, Y., Sounas, D. L. & Alù, A. Metagratings: beyond the limits of graded metasurfaces for wave front control. *Phys. Rev. Lett.* **119**, 067404 (2017).
74. Fan, Z. et al. Perfect diffraction with multiresonant bianisotropic metagratings. *ACS Photonics* **5**, 4303–4311 (2018).
75. Paniagua-Domínguez, R. et al. Generalized Brewster effect in dielectric metasurfaces. *Nat. Commun.* **7**, 10362 (2016).
76. Kamali, S. M. et al. Angle-multiplexed metasurfaces: encoding independent Wavefronts in a single metasurface under different illumination angles. *Phys. Rev. X* **7**, 041056 (2017).
77. Wenwei, L. et al. Metasurface enabled wide-angle Fourier lens. *Adv. Mater.* **30**, 1706368 (2018).
78. Qiu, M. et al. Angular dispersions in terahertz metasurfaces: physics and applications. *Phys. Rev. Appl.* **9**, 054050 (2018).
79. Backer, A. S. Computational inverse design for cascaded systems of metasurface optics. *Opt. Express* **27**, 30308–30331 (2019).
80. Pestourie, R. et al. Inverse design of large-area metasurfaces. *Opt. Express* **26**, 33732–33747 (2018).
81. Jensen, J. S. & Sigmund, O. Topology optimization for nano-photonics. *Laser Photonics Rev.* **5**, 308–321 (2011).
82. Lalau-Keraly, C. M., Bhargava, S., Miller, O. D. & Yablonovitch, E. Adjoint shape optimization applied to electromagnetic design. *Opt. Express* **21**, 21693–21701 (2013).
83. Molesky, S. et al. Inverse design in nanophotonics. *Nat. Photonics* **12**, 659–670 (2018).
84. Burger, M., Osher, S. J. & Yablonovitch, E. Inverse problem techniques for the design of photonic crystals. *IEICE Trans. Electron.* **87**, 258–265 (2004).
85. Miller, O. D. Photonic design: from fundamental solar cell physics to computational inverse design. Preprint at *arXiv* https://arxiv.org/abs/1308.0212 (2013).
86. Sell, D., Yang, J., Doshay, S., Yang, R. & Fan, J. A. Large-angle, multifunctional metagratings based on freeform multimode geometries. *Nano Lett.* **17**, 3752–3757 (2017).
87. Phan, T. et al. High-efficiency, large-area, topology-optimized metasurfaces. *Light Sci. Appl.* **8**, 48 (2019).
88. Byrnes, S. J., Lenef, A., Aieta, F. & Capasso, F. Designing large, high-efficiency, high-numerical-aperture, transmissive meta-lenses for visible light. *Opt. Express* **24**, 5110–5124 (2016).
89. Lin, Z., Liu, V., Pestourie, R. & Johnson, S. G. Topology optimization of freeform large-area metasurfaces. *Opt. Express* **27**, 15765–15775 (2019).
90. Zhang, H., Hsu, C. W. & Miller, O. D. Scattering concentration bounds: brightness theorems for waves. *Optica* **6**, 1321–1327 (2018).
91. Lin, Z. & Johnson, S. G. Overlapping domains for topology optimization of large-area metasurfaces. *Opt. Express* **27**, 32445–32453 (2019).
92. Torfeh, M. & Arbabi, A. Analysis and design of metasurfaces using the discrete-space impulse response technique. *Proc. SPIE High Contrast Metastruct. VIII* https://doi.org/10.1117/12.2510098 (2019).
93. Chung, H. & Miller, O. D. High-NA achromatic metalenses by inverse design. *Opt. Express* **28**, 6945–6965 (2020).
94. Aieta, F., Kats, M. A., Genevet, P. & Capasso, F. Multiwavelength achromatic metasurfaces by dispersive phase compensation. *Science* **347**, 1342–1345 (2015).
95. Chen, W. T. et al. A broadband achromatic metalens for focusing and imaging in the visible. *Nat. Nanotechnol.* **13**, 220–226 (2018).
96. Kempe, M., Stamm, U., Wilhelmi, B. & Rudolph, W. Spatial and temporal transformation of femtosecond laser pulses by lenses and lens systems. *J. Opt. Soc. Am. B* **9**, 1158–1165 (1992).
97. Weiner, A. M. in *Ultrafast Optics* (Wiley, 2008).
98. Almeida, V. R., Xu, Q., Barrios, C. A. & Lipson, M. Guiding and confining light in void nanostructure. *Opt. Lett.* **29**, 1209–1211 (2004).
99. Tong, L., Lou, J. & Mazur, E. Single-mode guiding properties of subwavelength-diameter silica and silicon wire waveguides. *Opt. Express* **12**, 1025–1035 (2004).
100. Wang, S. et al. A broadband achromatic metalens in the visible. *Nat. Nanotechnol.* **13**, 227–232 (2018).
101. Li, Y. et al. Achromatic flat optical components via compensation between structure and material dispersions. *Sci. Rep.* **6**, 19885 (2016).
102. Veronis, G. & Fan, S. Modes of subwavelength plasmonic slot waveguides. *J. Lightwave Technol.* **25**, 2511–2521 (2007).
103. Pu, M., Ma, X., Guo, Y., Li, X. & Luo, X. Theory of microscopic meta-surface waves based on catenary optical fields and dispersion. *Opt. Express* **26**, 19555–19562 (2018).
104. Shrestha, S., Overvig, A. C., Lu, M., Stein, A. & Yu, N. Broadband achromatic dielectric metalenses. *Light Sci. Appl.* **7**, 85 (2018).
105. Arbabi, E., Arbabi, A., Kamali, S. M., Horie, Y. & Faraon, A. Controlling the sign of chromatic dispersion in diffractive optics with dielectric metasurfaces. *Optica* **4**, 625–632 (2017).
106. Khorasaninejad, M. et al. Achromatic metalens over 60 nm bandwidth in the visible and metalens with reverse chromatic dispersion. *Nano Lett.* **17**, 1819–1824 (2017).
107. Shkondin, E. et al. Fabrication of high aspect ratio TiO_2 and Al_2O_3 nanogratings by atomic layer deposition. *J. Vac. Sci. Technol. A* **34**, 031605 (2016).
108. Zhou, Y. et al. Multifunctional metaoptics based on bilayer metasurfaces. *Light Sci. Appl.* **8**, 80 (2019).
109. Pu, M., Li, X., Guo, Y., Ma, X. & Luo, X. Nanoapertures with ordered rotations: symmetry transformation and wide-angle flat lensing. *Opt. Express* **25**, 31471–31477 (2017).
110. Yin, X. et al. Hyperbolic metamaterial devices for wavefront manipulation. *Laser Photonics Rev.* **13**, 1800081 (2019).
111. Poddubny, A., Iorsh, I., Belov, P. & Kivshar, Y. Hyperbolic metamaterials. *Nat. Photonics* **7**, 948–957 (2013).
112. Lin, R. J. et al. Achromatic metalens array for full-colour light-field imaging. *Nat. Nanotechnol.* **14**, 227–231 (2019).
113. Chen, N., Zuo, C., Lam, E. Y. & Lee, B. 3D imaging based on depth measurement technologies. *Sensors* **18**, 3711 (2018).
114. Fan, Z.-B. et al. A broadband achromatic metalens array for integral imaging in the visible. *Light Sci. Appl.* **8**, 67 (2019).
115. Hoffman, D. M., Girshick, A. R., Akeley, K. & Banks, M. S. Vergence–accommodation conflicts hinder visual performance and cause visual fatigue. *J. Vision* **8**, 33 (2008).
116. Liu, S. et al. A multi-plane optical see-through head mounted display design for augmented reality applications. *J. Soc. Inf. Display* **24**, 246–251 (2016).
117. Chen, W. T. et al. Broadband achromatic metasurface-refractive optics. *Nano Lett.* **18**, 7801–7808 (2018).
118. Stone, T. & George, N. Hybrid diffractive-refractive lenses and achromats. *Appl. Opt.* **27**, 2960–2971 (1988).
119. Sawant, R. et al. Mitigating chromatic dispersion with hybrid optical metasurfaces. *Adv. Mater.* **31**, 1805555 (2019).
120. Kurvits, J. A., Jiang, M. & Zia, R. Comparative analysis of imaging configurations and objectives for Fourier microscopy. *J. Opt. Soc. Am. A* **32**, 2082–2092 (2015).

121. Schuller, J. A. et al. Orientation of luminescent excitons in layered nanomaterials. *Nat. Nanotechnol.* **8**, 271–276 (2013).
122. Gao, N. et al. Ultra-dispersive anomalous diffraction from Pancharatnam-Berry metasurfaces. *Appl. Phys. Lett.* **113**, 113103 (2018).
123. Zhou, Y., Chen, R. & Ma, Y. Characteristic analysis of compact spectrometer based on off-axis meta-lens. *Appl. Sci.* **8**, 321 (2018).
124. Chen, W. T. et al. Integrated plasmonic metasurfaces for spectropolarimetry. *Nanotechnology* **27**, 224002 (2016).
125. Maguid, E. et al. Photonic spin-controlled multifunctional shared-aperture antenna array. *Science* **352**, 1202–1206 (2016).
126. Pors, A., Nielsen, M. G. & Bozhevolnyi, S. I. Plasmonic metagratings for simultaneous determination of Stokes parameters. *Optica* **2**, 716–723 (2015).
127. Camayd-Muñoz, P., Roberts, G., Debbas, M., Ballew, C. & Faraon, A. Inverse-designed spectrum splitters for color imaging. *Proc. Conf. Lasers Electro-Opt.* **AM4K**, AM4K.3 (2019).
128. Zhou, Y. et al. Multilayer noninteracting dielectric metasurfaces for multiwavelength metaoptics. *Nano Lett.* **18**, 7529–7537 (2018).
129. Lee, G.-Y. et al. Metasurface eyepiece for augmented reality. *Nat. Commun.* **9**, 4562 (2018).
130. Harm, W., Roider, C., Jesacher, A., Bernet, S. & Ritsch-Marte, M. Dispersion tuning with a varifocal diffractive-refractive hybrid lens. *Opt. Express* **22**, 5260–5269 (2014).
131. Colburn, S., Zhan, A. & Majumdar, A. Metasurface optics for full-color computational imaging. *Sci. Adv.* **4**, eaar2114 (2018).
132. Aiello, M. D. et al. Achromatic varifocal metalens for the visible spectrum. *ACS Photonics* **6**, 2432–2440 (2019).
133. Zhang, J., Zhang, L., Huang, K., Duan, Z. & Zhao, F. Polarization-enabled tunable focusing by visible-light metalenses with geometric and propagation phase. *J. Opt.* **21**, 115102 (2019).
134. Rubin, N. A. et al. Matrix Fourier optics enables a compact full-Stokes polarization camera. *Science* **365**, eaax1839 (2019).
135. Jang, M. et al. Wavefront shaping with disorder-engineered metasurfaces. *Nat. Photonics* **12**, 84–90 (2018).
136. Pahlevaninezhad, H. et al. Nano-optic endoscope for high-resolution optical coherence tomography in vivo. *Nat. Photonics* **12**, 540–547 (2018).
137. Guo, Q. et al. Compact single-shot metalens depth sensors inspired by eyes of jumping spiders. *Proc. Natl Acad. Sci. USA* **116**, 22959–22965 (2019).
138. Holsteen, A. L., Lin, D., Kauvar, I., Wetzstein, G. & Brongersma, M. L. A light-field metasurface for high-resolution single-particle tracking. *Nano Lett.* **19**, 2267–2271 (2019).
139. Capasso, F. The future and promise of flat optics: a personal perspective. *Nanophotonics* **7**, 953–957 (2018).
140. Faklis, D. & Morris, G. M. Polychromatic diffractive lens. US Patent US5589982A (1996).
141. Faklis, D. & Morris, G. M. Spectral properties of multiorder diffractive lenses. *Appl. Opt.* **34**, 2462–2468 (1995).
142. Arbabi, E., Arbabi, A., Kamali, S. M., Horie, Y. & Faraon, A. Multiwavelength polarization-insensitive lenses based on dielectric metasurfaces with meta-molecules. *Optica* **3**, 628–633 (2016).
143. Khorasaninejad, M. et al. Achromatic metasurface lens at telecommunication wavelengths. *Nano Lett.* **15**, 5358–5362 (2015).
144. Hu, T. et al. Demonstration of color display metasurfaces via immersion lithography on a 12-inch silicon wafer. *Opt. Express* **26**, 19548–19554 (2018).
145. Park, J.-S. et al. All-glass, large metalens at visible wavelength using deep-ultraviolet projection lithography. *Nano Lett.* **19**, 8673–8682 (2019).
146. She, A., Zhang, S., Shian, S., Clarke, D. R. & Capasso, F. Adaptive metalenses with simultaneous electrical control of focal length, astigmatism, and shift. *Sci. Adv.* **4**, eaap9957 (2018).
147. Ahn, S. H. & Guo, L. J. Large-area roll-to-roll and roll-to-plate nanoimprint lithography: a step toward high-throughput application of continuous nanoimprinting. *ACS Nano* **3**, 2304–2310 (2009).
148. Chen, X. et al. Plasmonic roller lithography. *Nanotechnology* **30**, 105202 (2019).
149. Geary, J. M. *Introduction to Lens Design: With Practical ZEMAX Examples* (Willmann-Bell, 2002).
150. Kamali, S. M., Arbabi, A., Arbabi, E., Horie, Y. & Faraon, A. Decoupling optical function and geometrical form using conformal flexible dielectric metasurfaces. *Nat. Commun.* **7**, 11618 (2016).
151. Wu, K., Coquet, P., Wang, Q. J. & Genevet, P. Modelling of free-form conformal metasurfaces. *Nat. Commun.* **9**, 3494 (2018).
152. Wilson, D. W., Maker, P. D., Muller, R. E., Mouroulis, P. Z. & Backlund, J. Recent advances in blazed grating fabrication by electron-beam lithography. *Proc. SPIE Curr. Dev. Lens Design Opt. Eng. IV* https://doi.org/10.1117/12.510204 (2003).
153. Arat, K. T. et al. Electron beam lithography on curved or tilted surfaces: Simulations and experiments. *J. Vac. Sci. Technol. B* **37**, 051604 (2019).
154. Jiang, J. et al. Free-form diffractive metagrating design based on generative adversarial networks. *ACS Nano* **13**, 8872–8878 (2019).
155. Jiang, J. & Fan, J. A. Global optimization of dielectric metasurfaces using a physics-driven neural network. *Nano Lett.* **19**, 5366–5372 (2019).
156. An, S. et al. Multifunctional metasurface design with a generative adversarial network. Preprint at *arXiv* https://arxiv.org/abs/1908.04851 (2019).
157. Engelberg, J. & Levy, U. The advantages of metalenses over diffractive lenses. *Nat. Commun.* **11**, 1991 (2020).
158. Decker, M. et al. Imaging performance of polarization-insensitive metalenses. *ACS Photonics* **6**, 1493–1499 (2019).
159. Banerji, S. et al. Imaging with flat optics: metalenses or diffractive lenses? *Optica* **6**, 805–810 (2019).
160. Banerji, S., Meem, M., Majumder, A., Sensale-Rodriguez, B. & Menon, R. Imaging over an unlimited bandwidth with a single diffractive surface. Preprint at *arXiv* https://arxiv.org/abs/1907.06251 (2019).
161. Banerji, S. et al. Single flat lens enabling imaging in the short-wave infra-red (SWIR) band. *OSA Continuum* **2**, 2968–2974 (2019).
162. Xie, Y.-Y. et al. Metasurface-integrated vertical cavity surface-emitting lasers for programmable directional lasing emissions. *Nat. Nanotechnol.* **15**, 125–130 (2020).
163. Huang, M. C. Y., Zhou, Y. & Chang-Hasnain, C. J. A surface-emitting laser incorporating a high-index-contrast subwavelength grating. *Nat. Photonics* **1**, 119–122 (2007).
164. Li, S.-Q. et al. Phase-only transmissive spatial light modulator based on tunable dielectric metasurface. *Science* **364**, 1087–1090 (2019).
165. Akselrod, G. M. Optics for automotive lidar: Metasurface beam steering enables solid-state, high-performance lidar. *LaserFocusWorld* https://www.laserfocusworld.com/optics/article/14036818/metasurface-beam-steering-enables-solidstate-highperformance-lidar (2019).
166. Luo, X. Subwavelength artificial structures: opening a new era for engineering optics. *Adv. Mater.* **31**, 1804680 (2019).
167. Li, X. et al. Dispersion engineering in metamaterials and metasurfaces. *J. Phys. D Appl. Phys.* **51**, 054002 (2018).
168. Li, W. & Fan, S. Nanophotonic control of thermal radiation for energy applications. *Opt. Express* **26**, 15995–16021 (2018).
169. Luo, X. Engineering optics 2.0: a revolution in optical materials, devices, and systems. *ACS Photonics* **5**, 4724–4738 (2018).
170. Pu, M., Guo, Y., Ma, X., Li, X. & Luo, X. Methodologies for on-demand dispersion engineering of waves in metasurfaces. *Adv. Opt. Mater.* **7**, 1801376 (2019).
171. Nemati, A., Wang, Q., Hong, M. & Teng, J. Tunable and reconfigurable metasurfaces and metadevices. *Opto-Electron. Adv.* **1**, 180009 (2018).
172. Cui, T., Bai, B. & Sun, H.-B. Tunable metasurfaces based on active materials. *Adv. Funct. Mater.* **29**, 1806692 (2019).
173. Zhang, S. et al. Solid-immersion metalenses for infrared focal plane arrays. *Appl. Phys. Lett.* **113**, 111104 (2018).
174. Ye, M., Ray, V. & Yi, Y. S. Achromatic flat subwavelength grating lens over whole visible bandwidths. *IEEE Photonics Technol. Lett.* **30**, 955–958 (2018).
175. Wang, S. et al. Broadband achromatic optical metasurface devices. *Nat. Commun.* **8**, 187 (2017).
176. Zhou, H., Chen, L., Shen, F., Guo, K. & Guo, Z. Broadband achromatic metalens in the midinfrared range. *Phys. Rev. Appl.* **11**, 024066 (2019).
177. Zhang, F., Zhang, M., Cai, J., Ou, Y. & Yu, H. Metasurfaces for broadband dispersion engineering through custom-tailored multi-resonances. *Appl. Phys. Express* **11**, 082004 (2018).
178. Zhao, F. et al. Optimization-free approach for broadband achromatic metalens of high-numerical-aperture with high-index dielectric metasurface. *J. Phys. D Appl. Phys.* **52**, 505110 (2019).
179. Yu, B., Wen, J., Chen, X. & Zhang, D. An achromatic metalens in the near-infrared region with an array based on a single nano-rod unit. *Appl. Phys. Express* **12**, 092003 (2019).
180. Lalanne, P. Waveguiding in blazed-binary diffractive elements. *J. Opt. Soc. Am. A* **16**, 2517–2520 (1999).
181. Wang, S. & Magnusson, R. Theory and applications of guided-mode resonance filters. *Appl. Opt.* **32**, 2606–2613 (1993).
182. Karagodsky, V., Sedgwick, F. G. & Chang-Hasnain, C. J. Theoretical analysis of subwavelength high contrast grating reflectors. *Opt. Express* **18**, 16973–16988 (2010).
183. Kuznetsov, A. I., Miroshnichenko, A. E., Brongersma, M. L., Kivshar, Y. S. & Luk'yanchuk, B. Optically resonant dielectric nanostructures. *Science* **354**, aag2472 (2016).
184. Lin, D., Fan, P., Hasman, E. & Brongersma, M. L. Dielectric gradient metasurface optical elements. *Science* **345**, 298–302 (2014).
185. Overvig, A. C., Shrestha, S. & Yu, N. Dimerized high contrast gratings. *Nanophotonics* **7**, 1157–1168 (2018).
186. Decker, M. et al. High-efficiency dielectric Huygens' surfaces. *Adv. Opt. Mater.* **3**, 813–820 (2015).
187. Pfeiffer, C. et al. Efficient light bending with isotropic metamaterial Huygens' surfaces. *Nano Lett.* **14**, 2491–2497 (2014).
188. Zheng, G. et al. Metasurface holograms reaching 80% efficiency. *Nat. Nanotechnol.* **10**, 308–312 (2015).
189. Verslegers, L. et al. Planar lenses based on nanoscale slit arrays in a metallic film. *Nano Lett.* **9**, 235–238 (2009).
190. Guo, Y. et al. Spoof plasmonic metasurfaces with catenary dispersion for two-dimensional wide-angle focusing and imaging. *iScience* **21**, 145–156 (2019).
191. Luo, X., Tsai, D., Gu, M. & Hong, M. Subwavelength interference of light on structured surfaces. *Adv. Opt. Photonics* **10**, 757–842 (2018).

Acknowledgements
This work was supported by the Defense Advanced Research Projects Agency (DARPA, grant no. HR00111810001). The authors thank Zhujun Shi for helpful discussion on topology optimization.

Author contributions
W.T.C. researched data for the article. W.T.C., A.Y.Z. and F.C. contributed to the discussion of content and wrote the article.

Competing interests
The authors declare no competing interests.

Publisher's note
Springer Nature remains neutral with regard to jurisdictional claims in published maps and institutional affiliations.

RELATED LINKS
A new centre of excellence for transformative meta-optical systems: https://www.arc.gov.au/2020-arc-centre-excellence-transformative-meta-optical-systems
DARPA extreme-optics programme: https://www.darpa.mil/program/extreme-optics-and-imaging
Leica Inc. developed an instrument for precise alignment of lenses: https://www.osa.org/en-us/meetings/webinar/older/values_of_microscope_objectives/
LightTrans: https://www.lighttrans.com/virtuallab-fusion-product-sheets/metalens-and-metasurface-holograms.html
Lux Research forecasted market opportunity in metamaterials: https://www.luxresearchinc.com/press-releases/lux-research-forecasts-10.7-billion-market-opportunity-in-metamaterial-devices
OSA incubator meeting of flat optics: https://www.osa.org/en-us/meetings/incubator_meetings/2020/flatopticsinc/
PlanOpSim: https://www.planopsim.com/
Samsung research award: https://www.sait.samsung.co.kr/saithome/about/collabo_apply.do
Sony research award: https://www.sony.com/research-award-program#FocusedResearchAward
Synopsys: https://www.synopsys.com/optical-solutions/rsoft/rsoft-product-applications/metalens_design_simulation_rsoft_codev.html
The World Economic Forum and Scientific American: https://www.scientificamerican.com/article/tiny-lenses-will-enable-design-of-miniature-optical-devices/
Zemax has teamed up with Lumerical: https://apps.lumerical.com/zemax-interoperability-metalens.html